Journal of Catalysis 395 (2021) 195–209

Contents lists available at ScienceDirect

Journal of Catalysis

journal homepage: www.elsevier.com/locate/jcat

Insight into the activity and SO_2 tolerance of hierarchically ordered $MnFe_{1-\delta}Co_{\delta}O_x$ ternary oxides for low-temperature selective catalytic reduction of NO_x with NH_3

Yonglong Li [a,1], Senyou Yang [a,1], Honggen Peng [a,b,*], Wenming Liu [a], Yangyang Mi [a], Zheng Wang [c], Changjin Tang [d], Daishe Wu [a], Taicheng An [b]

[a] College of Chemistry, Key Laboratory of Poyang Lake Environment and Resource Utilization, Ministry of Education, School of Resources Environmental and Chemical Engineering, Nanchang University, 999 Xuefu Road, Nanchang, Jiangxi 330031, China
[b] Guangdong Key Laboratory of Environmental Catalysis and Health Risk Control, School of Environmental Science and Engineering, Institute of Environmental Health and Pollution Control, Guangdong University of Technology, Guangzhou 510006, China
[c] State Key Laboratory of High-efficiency Utilization of Coal and Green Chemical Engineering, Ningxia University, Yinchuan, Ningxia 750021, China
[d] School of Environment, Nanjing Normal University, Nanjing 210023, China

ARTICLE INFO

Article history:
Received 10 August 2020
Revised 26 December 2020
Accepted 29 December 2020
Available online 6 January 2021

Keywords:
Nitrogen oxides
Low-temperature selective catalytic reduction
deNO_x
Hierarchically ordered catalysts
Ternary metal oxides

ABSTRACT

Manganese (Mn)-based mixed oxides are considered the most efficient catalysts for low-temperature ammonia selective catalytic reduction of nitrogen oxides (NO_x) (NH_3-SCR of NO_x). Water resistance and sulfur tolerance, especially the SO_2 tolerance of Mn-based catalysts, are the main obstacles preventing their practical application. Therefore, in this study, a series of cobalt (Co)-doped $MnFeO_x$ ternary mixed oxides catalysts with a hierarchically ordered structure (Hierc-$MnFe_{1-\delta}Co_{\delta}O_x$, δ = 0.2, 0.4 and 0.6) were developed and applied for NH_3-SCR of NO_x at low temperature. Compared with Hierc-$MnFeO_x$, Hierc-$MnFe_{1-\delta}Co_{\delta}O_x$ catalyst exhibited enhanced low-temperature activity and a broadened temperature window (NO_x conversion above 80% was between 90 and 343 °C over Hierc-$MnFe_{0.6}Co_{0.4}O_x$), as well as better H_2O resistance and SO_2 tolerance. The enhanced low-temperature activity was attributed to a larger amount of active oxygen species, a higher proportion of Mn^{4+}, Fe^{3+} and Co^{3+} content, and the improvement of surface acidity, which can facilitate the adsorption and activation of NO and NH_3. Additionally, the Hierc-$MnFe_{0.6}Co_{0.4}O_x$ catalyst exhibited superior soot tolerance due to its special hierarchically ordered architecture. In situ diffuse reflectance infrared Fourier transform spectroscopy (DRIFTS) revealed that the Co-modified Hierc-$MnFe_{1-\delta}Co_{\delta}O_x$ ternary oxide catalyst could efficiently protect nitrate species on Hierc-$MnFe_{0.6}Co_{0.4}O_x$ from the poisoning effect of SO_2, thereby boosting its SO_2 tolerance. This study provides a good candidate for low-temperature *de*NO_x application with enhanced SO_2 and soot tolerance.

1. Introduction

Nitrogen oxides (NO_x, x = 1, 2) as one of the main atmospheric pollutants discharged from vehicle and industrial sources, which can lead to acid rain, haze, and photochemical smog [1–5]. The NH_3 selective catalytic reduction (NH_3-SCR) of NO_x is a well-established method for elimination of NO_x due to its high activity and selectivity and low cost [4,6–9]. Vanadium/titanium-based catalysts have been used successfully in practical applications for many decades. However, they still have some disadvantages, such as narrow operating temperature (300–400 °C), lower activity at low temperature, and overoxidation of ammonia to nitrous oxide (N_2O) at high temperature [3,10–14]. Due to the high operating temperature, the SCR unit is placed upstream of the electrofiltration and devulcanization units, which leads to the rapid deactivation of catalysts due to the presence of H_2O and SO_2. To prevent or minimize their adverse impacts, it is possible to place *de*NO_x catalysts downstream of the electrofilter and devulcanizer. However, the flue gas temperature will be too low to reach the working temperature window of the vanadium/titanium-based catalyst [15]. In addition, small amounts of particulate matter, such as soot, may

* Corresponding author at: College of Chemistry, Key Laboratory of Poyang Lake Environment and Resource Utilization, Ministry of Education, School of Resources Environmental and Chemical Engineering, Nanchang University, 999 Xuefu Road, Nanchang, Jiangxi 330031, China.
E-mail address: penghonggen@ncu.edu.cn (H. Peng).
[1] These authors contributed equally to this work.

https://doi.org/10.1016/j.jcat.2020.12.036
0021-9517/

still exist in flue gas and can cover the active sites of the *de*NO_x catalysts. Therefore, it is necessary to design and prepare vanadium-free *de*NO_x catalysts with excellent low-temperature (< 250 °C) activity and strong resistance to H_2O/SO_2 and particulate matter.

Currently, numerous vanadium-free transition metal or mixed metal oxide catalysts have been shown to be active for NH_3-SCR of NO_x [16–19]. Manganese (Mn)-based catalysts have been investigated intensively due to their superior low-temperature performance [15,20–25]. However, pure Mn oxides (MnO_x) are readily poisoned by SO_2 and H_2O. In recent years, an increasing number of studies have shown that bimetallic Mn–Fe catalysts have fairly good performance in NH_3-SCR, but their low-temperature activity, especially their H_2O/SO_2 tolerance, is still unsatisfactory [15,22,26,27]. Recent studies have demonstrated that MnO_x properly doped with cobalt oxide (CoO_x) displays excellent catalytic performance and SO_2 tolerance, which are attributed to the synergistic effect of Co and Mn [28–31]. Additionally, the particle size of particulate matter (> 25 nm) is often greater than that of the pores of conventional *de*NO_x catalysts; thus, the surface-active sites can be covered readily, resulting in performance degradation.

Materials with hierarchically ordered structure, such as three-dimensional hierarchically ordered macroporous metal oxide catalysts with uniform large pore diameter (> 50 nm), have attracted a considerable amount of interest in environmental catalysis [32–35]. In this study, a series of Co-modified $MnFeO_x$ with hierarchically ordered structure (Hierc-$MnFe_{1-\delta}Co_\delta O_x$, δ = 0.2, 0.4 and 0.6) were developed to overcome the various obstacles (including weak tolerance of H_2O, SO_2 and soot) preventing the practical application of Mn-based mixed metal oxides for low-temperature NH_3-SCR of NO_x. Various techniques were adopted to investigate the effects of Co addition on the catalytic performance of the Hierc-$MnFe_{1-\delta}Co_\delta O_x$ catalyst. Our results demonstrated that the Hierc-$MnFe_{0.6}Co_{0.4}O_x$ catalysts have superior low-temperature activity, which can be attributed to its higher surface Mn^{4+} (and Fe^{3+}, Co^{3+}) concentration, larger ratio of surface chemical adsorption oxygen species, and greater acid amount. The SO_2/H_2O/soot tolerance and the reaction mechanism over the Hierc-$MnFe_{0.6}Co_{0.4}O_x$ catalyst were also studied in detail. The Co-modified ternary oxide catalysts with hierarchically ordered structure developed in this work provide a good example for researchers in this field to design and synthesize high-performance low-temperature *de*NO_x catalysts with improved H_2O, SO_2 and soot tolerance for practical applications. An illustration of the synthesis of the hierarchically ordered Hierc-$MnFe_{1-\delta}Co_\delta O_x$ (δ = 0.2, 0.4 and 0.6) catalyst and its application in the NH_3-SCR of NO_x is displayed in Scheme 1.

2. Experimental

2.1. Catalyst preparation

2.1.1. Synthesis of Hierc-$MnFe_{1-\delta}Co_\delta O_x$ (δ = 0.2, 0.4 and 0.6)

All reagents were analytical grade and used as received without further purification. Homogeneously dispersed polymer nanospheres (polymethyl methacrylate, PMMA) were synthesized according to a method described elsewhere [36]. In a typical synthesis of Hierc-$MnFe_{0.6}Co_{0.4}O_x$, 2.0 g (0.1538 mmol) of F127 surfactant (from Sigma-Aldrich, 99%) and 4.0 g (19.0349 mmol) of citric acid monohydrate (from Aladdin, 99.5%) as mixture were added to an ethylene glycol (from Xilong Scientific, 99%) and methanol (from Xilong Scientific, 99.5%) solution (40 vol%) and stirred for 2 h to form a uniform precursor solution. Then 50 mmol Mn $(NO_3)_2$ (50 wt%, from Macklin), 30 mmol $Fe(NO_3)_3{\cdot}9H_2O$ (from Xilong Scientific, 98.5%), and 20 mmol $Co(NO_3)_2{\cdot}6H_2O$ (from Xilong Scientific, 98.5%) were dissolved in the solution to obtain a transparent solution under vigorous stirring at 35 °C for 5 h. The total metal concentration for each precursor solution was 2 mol L^{-1}. The PMMA nanospheres were soaked for 6 h in the above solution; after the PMMA template was fully impregnated, vacuum filtration was carried out to remove the excessive metal precursor solution. The precipitates were dried at 50 °C in a vacuum oven for 48 h and first calcined at 310 °C in N_2 for 4 h, and then calcined in a tube furnace at a rising rate of 1 °C min^{-1} to 550 °C in air and held for 5 h to remove the PMMA hard template and the F127 soft template. Afterwards the desired Hierc-$MnFe_{0.6}Co_{0.4}O_x$ was obtained. According to the same procedure, Hierc-$MnFe_{1-\delta}Co_\delta O_x$ catalysts with various Co content were prepared, and the molar ratio Mn:Fe:Co was fixed at 1:1-δ :δ (δ = 0.2, 0.4 and 0.6). Pure Hierc-MnO_x, Hierc-FeO_x, Hierc-CoO_x and Hierc-$MnFeO_x$ were also synthesized using the same method.

2.1.2. Synthesis of Con-$MnFe_{0.6}Co_{0.4}O_x$ catalysts

For comparison, an $MnFe_{0.6}Co_{0.4}O_x$ catalyst without a hierarchical ordered structure was also prepared by the conventional method (denoted as Con-$MnFe_{0.6}Co_{0.4}O_x$). Typically, proper amounts of $Mn(NO_3)_2$, $Fe(NO_3)_3{\cdot}9H_2O$, and $Co(NO_3)_2{\cdot}6H_2O$ precursors were mechanically mixed to form a homogeneous solution; then the complexing agent was dried and calcined, and the procedures used were the same as above.

2.2. Catalyst characterization

Various characterization techniques were adopted to measure the physicochemical performance of Hierc-$MnFe_{1-\delta}Co_\delta O_x$ (δ = 0.2, 0.4 and 0.6) and related catalysts. Field-emission scanning electron microscopy (SEM) images, transmission electron microscopy (TEM) images, and elemental mapping images were obtained using a JEOL 3000F TEM working at 300 kV equipped with an energy-dispersive spectroscopy (EDS) detector. X-ray diffraction (XRD) patterns were recorded on a Bruker AXS D8Focus diffractometer that operated at 40 kV and 30 mA with a Cu target and *K*α-ray irradiation (λ = 1.54178 Å). Scans were collected in the 2θ range from 10° to 80° with a step of 2° min^{-1} to analyze the phase structure. Nitrogen adsorption–desorption analysis was carried out at 77 K on a Micromeritics ASAP2020 instrument. The specific surface areas of the samples were calculated using the Brunauer–Emmett–Teller (BET) method. The pore size distributions of the samples were calculated according to the Barrett–Joyner–Halenda (BJH) method. The average pore sizes of the samples were obtained from the peak positions of the distribution curves. X-ray photoelectron spectroscopy (XPS) was performed on a PHI 5000 Versa Probe high performance electron spectrometer using monochromatic aluminum *K*α radiation (1486.6 eV) at an accelerating power of 15 kW. Before the measurement, the sample (50 mg) was treated in an O_2 flow of 20 mL min^{-1} at 200 °C for 1 h; then the sample was outgassed at room temperature in a UHV chamber (1.0×10^{-9} Torr). The sample charging effects were compensated for by calibrating all binding energies (BE) with the adventitious C 1s peak at 284.5 eV. The BE values of Fe 2p, Mn 2p, Co 2p and O 1s were calibrated against the C 1s signal (BE = 284.5 eV) of contaminant carbon. Temperature-programmed reduction by hydrogen (H_2-TPR) was carried out on a FINESORB 3010C instrument in a 30 mL min^{-1} 10% H_2–Ar gas flow, with the temperature increased from room temperature to 950 °C at 10 °C min^{-1} after pretreatmen at 300 °C for 30 min in flowing N_2. Generally, 50 mg of catalyst was used for this test. Temperature-programmed desorption of NH_3 (NH_3-TPD) was carried out via a Micromeritics ASAP 2920. After the samples were pretreated in pure Ar at 400 °C for 1 h, the adsorption of NH_3 was conducted at 50 °C for 1 h, followed by purging with Ar. Finally, the samples were heated from 50 to 500 °C with a ramping rate of 10 °C min^{-1}. The reaction mechanism was studied by *in situ* DRIFT measurement on a Fourier trans-

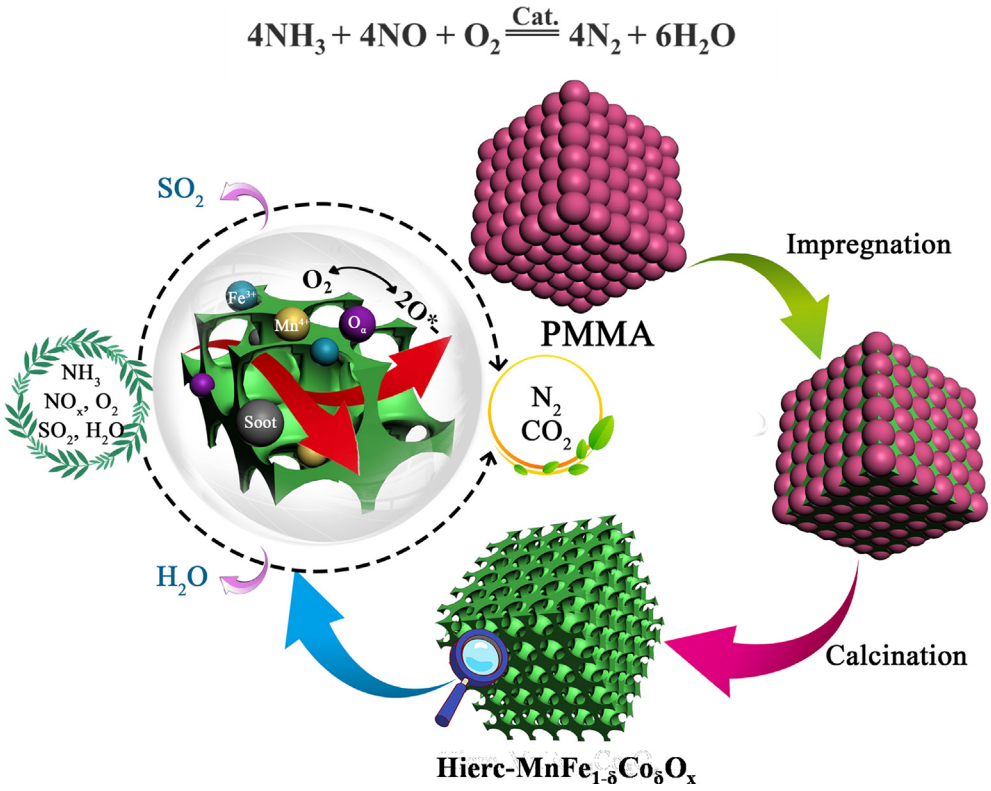

Scheme 1. Illustration of the hierarchically ordered Hierc-$MnFe_{1-\delta}Co_{\delta}O_x$ (δ = 0.2, 0.4 and 0.6) catalyst: synthesis and application in NH_3-SCR of NO_x.

form infrared spectrometer (Bruker Tensor 27) equipped with a Pike DRIFT cell (DiffusIR) and a mercury cadmium telluride (MCT) detector cooled by liquid nitrogen. For each test, the samples were pretreated for 60 min in a N_2 flow at 400 °C and cooled to target temperature under N_2 flow. All DRIFT spectra were recorded by accumulating 64 scans, at a resolution of 4 cm^{-1}, as a function of time. Gas flow was controlled by a gas mass controller (Sevenstar, China) and the gas feeds used for the experiment were a mixture of 500 ppm of NH_3/N_2, 500 ppm of NO + 5% O_2/N_2 and 100 ppm of SO_2 + 5% O_2/N_2 when used.

2.3. Catalytic and kinetic tests

The *de*NO_x performance of the as-prepared catalysts was evaluated on a fixed-bed tubular quartz system (ID = 6 mm). The feed gas mixture contained 500 ppm of NO, 500 ppm of NH_3, 5% of O_2, 5% of H_2O (when used), 100 ppm of SO_2 (when used), and N_2 as balance gas with a total flow rate of 100 mL min^{-1}, and the weight hourly space velocity (WHSV) was set at 60,000 mL $g_{cat.}^{-1}$ h^{-1}. Prior to the measurement of activity, 100 mg of catalyst was swept using a flow of 100 mL min^{-1} N_2 at 300 °C for 1 h to remove the physisorbed H_2O; then the background infrared (IR) spectrum of the reactor effluent was recorded under nitrogen at room temperature. Thereafter, the IR spectra of the effluent of the reactor simulated feed were recorded for half an hour. Catalytic activity performance measurements were conducted by heating the fixed bed at a rate of 3 °C min^{-1}. The composition and concentration of the outlet gas were continually monitored by Fourier transform infrared (FT-IR) spectroscopy using a Nicolet Antaris IGS-Gas Analyzer (Thermo Fisher Scientific, Waltham, MA) equipped with a 2-m length gas cell.

The conversion of NO_x and selectivity for N_2 were calculated according to the equations

$$X_{NO_x} = \left(1 - \frac{[NO_x]_{outlet}}{[NO_x]_{inlet}}\right) \times 100\%, \quad (1)$$

$$N_2 selectivity = \left(1 - \frac{2[N_2O]_{outlet}}{[NO_x]_{inlet} - [NO_x]_{outlet} + [NH_3]_{inlet} - [NH_3]_{outlet}}\right) \times 100\%, \quad (2)$$

where X_{NO_x} is the conversion of NO_x at a certain temperature (%), $[NO_x]$ = $[NO]$ + $[NO_2]$, and $[NO_x]_{inlet}$ and $[NO_x]_{outlet}$ are the inlet and outlet gas concentrations of NO_x, respectively.

The kinetic performance of Hierc-$MnFe_{0.6}Co_{0.4}O_x$ and related catalysts was evaluated by calculating the apparent activation energy (E_a) and turnover frequency (TOF) for NO_x conversion. The NH_3-SCR kinetic measurements over different as-prepared catalysts were conducted in a quartz reactor. To that end, a sample of 25 mg of the catalyst and 75 mg of inert quartz sand (40–60 mesh) were packed in a quartz tube (ID 6 mm). The reaction gases contained 500 ppm of NO, 500 ppm of NH_3, 5% O_2, and N_2 as balance gas, with a total flow rate of 400 mL min^{-1}; the WHSV was fixed at 960,000 mL $g_{cat.}^{-1}$ h^{-1}; and the NO_x conversion rate was kept at less than 10%. Low conversion of NO_x and the absence of mass and heat transfer limitations ensure the reaction in the kinetic region. (The influences of mass transport limitation and heat transfer were excluded by calculating the Weisz–Prater criterion and the Mears criterion, respectively [37–39]. The detailed calculations are shown in the Supporting Information.) The normalized reaction rate, R_{NO_x}(mol $g_{cat.}^{-1}$ s^{-1}), was calculated using the formula

$$R_{NO_x} = \frac{X_{NO_x} V}{m_{cat.}}, \quad (3)$$

where V is the gas flow rate (mol s^{-1}) of NO_x and $m_{cat.}$ is the mass weight of the sample. The apparent activation energy (E_a, in kJ

mol^{-1}) can be obtained from the Arrhenius plots of the reaction rate. In addition, the turnover frequency (TOF) value (based on active species, such as Mn, Fe and Co) per second was used to compare the intrinsic catalytic activity of the catalysts [40]. The calculation equations are

$$\mathrm{TOF} = \frac{v \times X_{NO_x}}{V_m \times n_{(Mn+Fe+Co)-surf.}}, \quad (4)$$

where v is the flow rate of NO_x ($m^3\ s^{-1}$); V_m is the gas molar constant ($m^3\ mol^{-1}$); and $n_{(Mn+Fe+Co)-surf.}$ is the total mole number of atoms on the surfaces of catalysts (mol), which is estimated from the N_2 adsorption/desorption and XPS data,

$$n_{(Mn+Fe+Co)-surf.} = \frac{N_{(Mn+Fe+Co)-surf.}}{N_A}, \quad (5)$$

$$N_{(Mn+Fe+Co)-surf.} = N_{Mn-surf.} + N_{Fe-surf.} + N_{Co-surf.}, \quad (6)$$

where $N_{(Mn+Fe+Co)-surf.}$ is the number of atoms on the surfaces of catalysts and N_A is the Avogadro constant ($6.02\times10^{23}\ mol^{-1}$).

The calculation formulas for $N_{(Mn+Fe+Co)-surf.}$ are

$$m \cdot S_{BET} = S_{Mn-surf.} + S_{Fe-surf.} + S_{Co-surf.} + S_{O-surf.}$$

$$= N_{Mn-surf.} \cdot S_{Mn-single} + N_{Fe-surf.} \cdot S_{Fe-single}$$

$$+ N_{Co-surf.} \cdot S_{Co-single} + N_{O-surf.} \cdot S_{O-single}, \quad (7)$$

where m (g) is the mass of catalysts used for XPS analysis (50 mg); S_{BET} ($m^2\ g^{-1}$) is the surface area of catalysts (Table S2 in the Supporting Information); and $S_{Mn-single}$ (m^2), $S_{Fe-single}$ (m^2), $S_{Co-single}$, and $S_{O-single}$ (m^2) are the surface areas of single atoms, which were estimated by the hemispheric surface area ($2\pi r^2$). The atomic radii employed for Mn, Fe, Co and O are as follows:

$$r_{Mn} = 1.24 \times 10^{-10}\ \mathrm{m},\ r_{Fe} = 1.289 \times 10^{-10}\ \mathrm{m},$$
$$r_{Co} = 1.253 \times 10^{-10}\ \mathrm{m},\ \text{and}\ r_O = 6.4 \times 10^{-11}\ \mathrm{m}.$$

The relationship between $N_{Mn-surf.}$, $N_{Fe-surf.}$ and $N_{Co-surf.}$was calculated based on the XPS analysis results; relevant values are listed in Table S3.

The evaluation of the soot resistance capacity was also undertaken in the same quartz reactor. Commercially obtained Printex-U (diameter ~25 nm, purchased from Degussa) was chosen as model particulate matter (soot). Typically, the as-prepared catalyst (100 mg) and soot (10 mg) were mixed at a weight ratio of 10:1 with a spatula to duplicate the loose contact condition. The detailed reaction measurement procedures were similar to those described above.

3. Results and discussion

3.1. Catalytic performance

The performance of Hierc-$MnFeO_x$, Hierc-$MnFe_{0.6}Co_{0.4}O_x$, and three pure metal oxide catalyst for *de*NO_x is displayed in Fig. 1a. The pure Hierc-FeO_x catalyst exhibited the worst *de*NO_x performance, as only 40% NO_x conversion was achieved at 300 °C. The *de*NO_x activity was also poor in the presence of Hierc-CoO_x, yielding 63% NO_x conversion at around 310 °C. Intriguingly, Hierc-CoO_x showed a second peak in its activity curves (centered at 310 °C), which is consistent with previous studies suggesting that this catalyst follows different reaction mechanisms in different temperature windows [41,42]. However, Hierc-MnO_x showed better activity than Hierc-FeO_x and Hierc-CoO_x, achieving above 80% NO_x conversion over a narrow temperature window from 175 to 275 °C. The Hierc-$MnFeO_x$ catalyst exhibited better low-temperature activity with a wider temperature window than Hierc-MnO_x. Remarkably, the NO_x conversion was greatly improved after the doping of Co into Hierc-$MnFeO_x$. The Hierc-$MnFe_{0.6}Co_{0.4}O_x$, in particular, with an Fe/Co molar ratio of 6 to 4, showed the best *de*NO_x activity, especially low-temperature activity, in which its 100% NO_x conversion was as low as 150 °C and its temperature window (NO_x conversion > 80%) ranged from 90 to 343 °C. With increasing cobalt species doping amount, the activity decreased but was still higher than that of Hierc-$MnFeO_x$ (Fig. 1b). There is an optimal amount of cobalt doping for Hierc-$MnFe_{1-\delta}Co_\delta O_x$ ternary oxide catalysts, and excessive Co doping was not conducive to enhance its NH_3-SCR activity. It should be noted that hierarchically ordered Hierc-$MnFe_{0.6}Co_{0.4}O_x$ exhibited enhanced performance compared with conventional $MnFe_{0.6}Co_{0.4}O_x$ without an ordered hierarchical structure (Fig. S1), which could be ascribed to the ordered porous structure that could promote the transportation of the reactants and products.

To achieve the fully significant effects of cobalt in the Hierc-$MnFe_{0.6}Co_{0.4}O_x$ catalyst, separate NO oxidation (500 ppm of NO + 5% of O_2) and NH_3 oxidation (500 ppm of NH_3 + 5% of O_2) reactions were performed. As shown in Fig. 1c, the concentration of NO_2 concentration over Hierc-$MnFe_{0.6}Co_{0.4}O_x$ was evidently far higher than that over Hierc-$MnFeO_x$ in the whole temperature range. It has been reported that if the SCR catalysts could produce a fraction of NO_2 in situ from NO oxidation at low temperature, the low-temperature SCR activity would be increased via the "fast SCR" process in Eq. (8) [43].

$$2NO + 2NO_2 + 4NH_3 = 4N_2 + 6H_2O. \quad (8)$$

NO_2 is a better oxidizing agent than O_2; NO_2 reacts directly with the reduced site, resulting in a higher rate for the fast SCR reaction at low temperatures [44–46].

In the actual SCR reaction, the surface reaction between nitrate species and NH_3 adsorbed species is dominant in the SCR reaction; therefore, Hierc-$MnFe_{0.6}Co_{0.4}O_x$ has a higher NO oxidation ability, which accounts for its better low-temperature NH_3-SCR activity than that of Hierc-$MnFeO_x$. Moreover, the processes of NH_3 activation and oxidation are vital for the NH_3-SCR reaction, and the relevant results of NH_3 oxidation are shown in Fig. 1d, where the NH_3 oxidation activity over Hierc-$MnFe_{0.6}Co_{0.4}O_x$ is much lower than that over Hierc-$MnFeO_x$. For the Hierc-$MnFe_{0.6}Co_{0.4}O_x$ catalyst, the NH_3 oxidation started at ~225 °C, but approximately total conversion (~96%) of NH_3 could be accomplished at the same temperature over the Hierc-$MnFeO_x$ catalyst. This indicates that the introduction of cobalt into Hierc-$MnFeO_x$ can effectively suppress NH_3 oxidation, which accounted for its superior catalytic activity and excellent N_2 selectivity. Meanwhile, as the other important indicators of catalytic performance, as shown in Fig. S2a, N_2 selectivity was provided, suggesting that the introduction of cobalt could also suppress the side reactions in the NH_3-SCR process. Hierc-$MnFe_{0.6}Co_{0.4}O_x$ had higher N_2 selectivity than the Hierc-$MnFeO_x$ catalyst, and its N_2 selectivity was about 80% even when the reaction temperature reached 300 °C. The N_2 selectivity for Hierc-$MnFeO_x$ was only 70% at 300 °C. Furthermore, Hierc-$MnFe_{0.6}Co_{0.4}O_x$ was more conducive to the reaction of ammonia in the NH_3-SCR process (Fig. S2b). The conversion of NO to NO_2, N_2O, and N_2 is shown in Fig. S3, and the results were consistent with the better N_2 selectivity over the Hierc-$MnFe_{0.6}Co_{0.4}O_x$ catalyst. The above results suggested that Co doping had a major effect in enhancing the performance of the Hierc-$MnFe_{0.6}Co_{0.4}O_x$ catalyst in the NH_3-SCR reaction. Further study of the catalytic stability over Hierc-$MnFe_{0.6}Co_{0.4}O_x$ at 165 °C revealed, as shown in Fig. S4a, a decrease of only 4% conversion throughout the continuous 20 h of testing. It should be noted that when the heating steps in the testing method are changed (first, the temperature increased to 450 °C, and then decreased to room temperature, and ultimately increased to 450 °C again), a smooth curve is also obtained. This

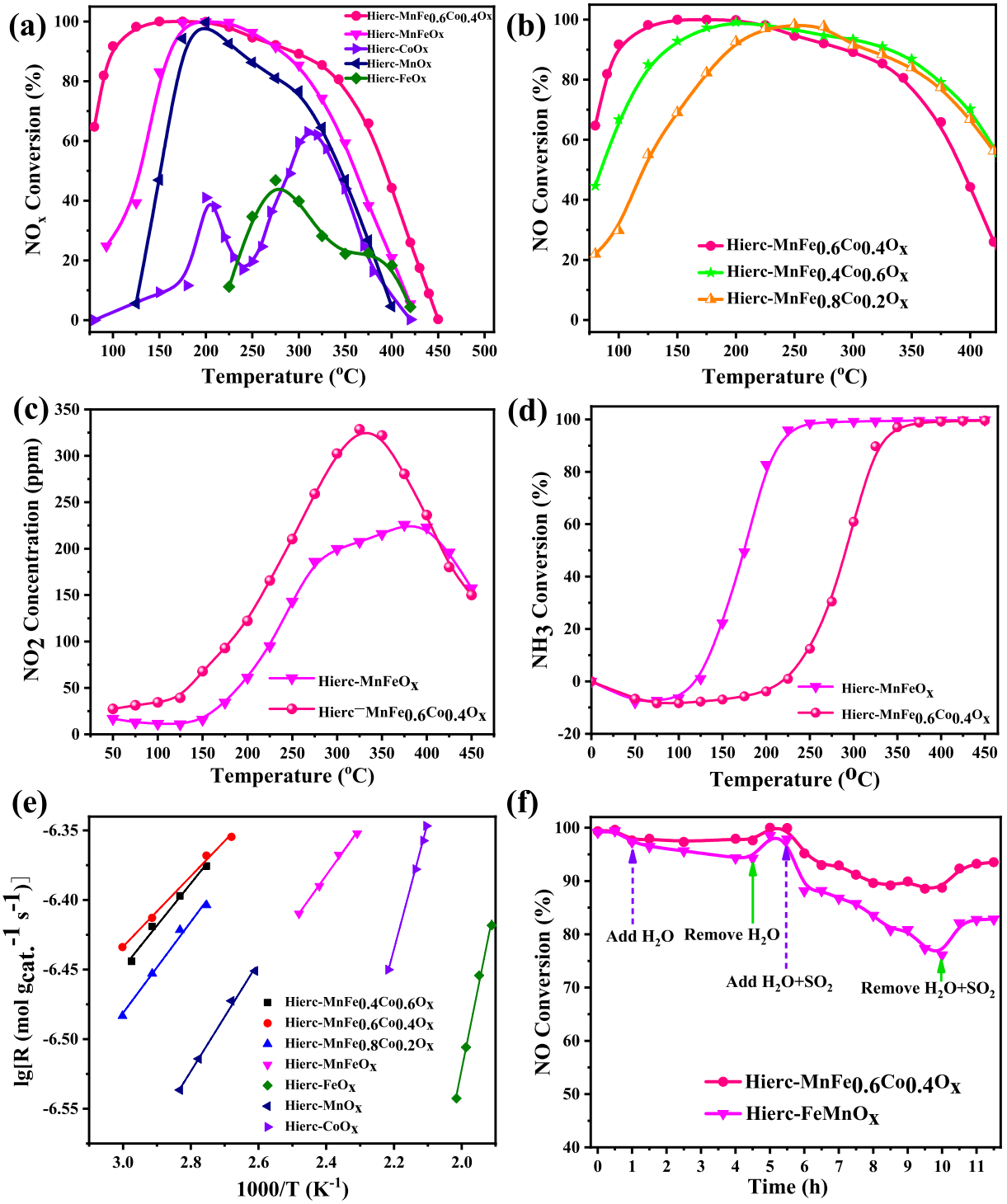

Fig. 1. (a) NO_x conversion as a function of temperature in the NH_3-SCR reaction over Hierc-$MnFe_{0.6}Co_{0.4}O_x$ and related catalysts; (b) NO_x conversion as a function of temperature in the NH_3-SCR reaction over Hierc-$MnFe_{0.8}Co_{0.2}O_x$, Hierc-$MnFe_{0.6}Co_{0.4}O_x$ and Hierc-$MnFe_{0.4}Co_{0.6}O_x$ catalysts; (c) The separate NO oxidation reactions results over Hierc-$MnFe_{0.6}Co_{0.4}O_x$ and Hierc-$MnFeO_x$ catalysts; (d) The separate NH_3 oxidation reactions results over Hierc-$MnFe_{0.6}Co_{0.4}O_x$ and Hierc-$MnFeO_x$ catalysts; (e) Arrhenius curves of NH_3-SCR over various catalysts; (f) Effect of H_2O/SO_2 on NO_x conversion over Hierc-$MnFe_{0.6}Co_{0.4}O_x$ and Hierc-$MnFeO_x$ catalysts at 180 °C.

clearly indicated that the catalyst did not change with temperature (Fig. S4b). The above two experimental results indicated that Hierc-$MnFe_{0.6}Co_{0.4}O_x$ had excellent thermal stability.

The apparent E_a of a catalytic reaction is an important parameter to assess an industrial catalyst [47,48]. Therefore, the reaction kinetics of the as-prepared samples for SCR of NO_x with NH_3 were studied before the heat and mass transfer limits were excluded (confirmed by the Weisz–Prater criterion and the Mears criterion calculation; see the Supporting Information). The Arrhenius curves and activity curves at high space velocity are shown in Fig. 1e and Fig. S5, respectively. The E_a and TOF values are listed in Table S1. These results indicated that mono-metal oxides and $MnFeO_x$ catalysts had a higher E_a value than that of the ternary $MnFe_{1-\delta}Co_\delta O_x$ catalysts, while the Hierc-$MnFe_{0.6}Co_{0.4}O_x$ catalyst had the lowest E_a value, indicating that the addition of Co into Hierc-$MnFeO_x$ effectively reduced the E_a and enhanced the *de*NO_x performance. Also, the higher TOF values

of Hierc-$MnFe_{0.6}Co_{0.4}O_x$ than that of Hierc-$MnFeO_x$ further confirm the excellent low-temperature *de*NO_x efficiency of the former.

In practical applications, the flue gases often include small amounts of H_2O and SO_2, which result in poisoning and deactivation of *de*NO_x catalysts. Accordingly, investigating the effect of H_2O/SO_2 is critical in the use of *de*NO_x catalysts. The influence of H_2O and SO_2 on Hierc-$MnFe_{0.6}Co_{0.4}O_x$ and Hierc-$MnFeO_x$ was evaluated at 180 °C. The results, displayed in Fig. 1f, revealed that the activity decreased slowly after 5 vol% H_2O was introduced over Hierc-$MnFe_{0.6}Co_{0.4}O_x$, which can be attributed to the comparative adsorption of NH_3 and H_2O [49,50]. It was also noticed that Hierc-$MnFeO_x$ had a large sharp decrease in activity compared with Hierc-$MnFe_{0.6}Co_{0.4}O_x$. Additionally, the NO_x conversion returned to about 98% soon after the H_2O was removed, suggesting the strong H_2O tolerance of Hierc-$MnFe_{0.6}Co_{0.4}O_x$. Furthermore, the evaluation of the effect of the co-presence of SO_2 and H_2O revealed that the catalyst activity apparently decreased over the Hierc-$MnFeO_x$ catalyst, noticeably, the NO_x conversion declined from 98% to 76%. However, the decline was slight over Hierc-$MnFe_{0.6}Co_{0.4}O_x$, in which the NO_x conversion only declined from 99% to 88%. The deactivation over Hierc-$MnFe_{0.6}Co_{0.4}O_x$ and Hierc-$MnFeO_x$ was mainly attributed to the deposition of sulfate species, such as NH_4HSO_4, $(NH_4)_2SO_4$, and metal sulfates [12]. When the addition of H_2O and SO_2 were turned off, the NO_x conversion over Hierc-$MnFeO_x$ and Hierc-$MnFe_{0.6}Co_{0.4}O_x$ could be partially recovered to 82% and 93%, respectively. The above results indicated that the H_2O tolerance, and especially the SO_2 tolerance of the catalyst could be enhanced significantly by the doping of the cobalt into the $MnFeO_x$ catalyst. The resistance to water vapor and sulfur dioxide tests were further performed at lower temperature (120 °C), as shown in Fig. S6, adding cobalt into Hierc-$MnFeO_x$ could effectively retard the sulfur poisoning, however, the performance of resistance to SO_2 needs to be further improved at 120 °C.

Since the soot emitted from flue gases can cover the active sites of the *de*NO_x catalyst, the soot resistance performance was tested using a commercial soot nanoparticle as a model (~25 nm). The results presented in Fig. 2 clearly showed a sharp decrease in *de*NO_x activity over the mixture of the carbon and the Con-$MnFe_{0.6}Co_{0.4}O_x$ catalyst without a hierarchically ordered structure prepared by the conventional method. However, the NO_x conversion–temperature curve from 150 to 250 °C over Hierc-$MnFe_{0.6}Co_{0.4}O_x$ was almost coincident even though the soot was added to the catalyst. These results revealed that the Hierc-$MnFe_{0.6}Co_{0.4}O_x$ had excellent soot resistance compared with Con-$MnFe_{0.6}Co_{0.4}O_x$ due to its special hierarchically ordered structure, which might prevent the impact of the carbon covering the surface-active sites with carbon. Noticeably, after soot was introduced, the *de*NO_x activity at high temperature was enhanced for both Con-$MnFe_{0.6}Co_{0.4}O_x$ and Hierc-$MnFe_{0.6}Co_{0.4}O_x$. Additional experiments were conducted to investigate the cause of the enhanced activity. As shown in Fig. S7, in the absence of NH_3, the concentration of NO_x decreased gradually and reached a minimum at about 400 °C, and simultaneously, the concentration of CO_2 increased and reached a maximum at about 400 °C. As the temperature increased further, the concentration of NO_x increased and ultimately reached a plateau, while the concentration of CO_2 declined and eventually became completely undetectable. Thus, the overall chemical reaction equation could be written as

$$3C + 4NO + O_2 = 2N_2 + 3CO_2 \quad (9)$$

Additionally, as shown in Fig. S8, in the absence of NH_3 and O_2, the conversion of NO_x was gradually increased at 300–650 °C, while the conversion of NO_x increased rapidly with the increasing temperature, ultimately 97% NO_x conversion was achieved at 800 °C. It is worth noting that the CO_2 concentration increased concurrently. Also, a blank test was performed to elucidate the probability of NO_x decomposition at high reaction temperature, and it was found that the NO_x could not be decomposed even as the temperature increased to 850 °C. Therefore, the general chemical reaction equation was determined to be

$$2C + 4NO = 2N_2 + 2CO_2. \quad (10)$$

The above results demonstrated that the soot particles could act as a reductant to reduce NO_x over Hierc-$MnFe_{0.6}Co_{0.4}O_x$ and eventually led to the improvement of the high-temperature *de*NO_x performance. Remarkably, from another perspective, in this work, it was possible to remove NO_x and soot simultaneously.

3.2. Scanning electron microscopy and transmission electron microscopy analysis of the catalysts

The morphology and hierarchically ordered structure of Hierc-$MnFe_{0.6}Co_{0.4}O_x$ and the related catalysts were confirmed by scanning electron microscopy (SEM). The image shown in Fig. S9 indicated that the as-synthesized PMMA nanospheres with particle size about 210 nm had been successfully prepared and thus they were used as a hard template to synthesize the hierarchically ordered catalysts. The representative SEM images of the catalysts displayed in Fig. 3 revealed that all the as-prepared catalysts exhibited a high-quality hierarchically ordered structure with a macropore size of 110–140 nm. The macropores were connected by small windows in a highly ordered way. These results suggested that the hierarchically ordered structure was achieved by PMMA microspheres as the hard template. Noticeably, compared with the initial particle size (210 nm) of PMMA nanospheres, the diameter of these macropores decreased to 110–140 nm owing to the melting of PMMA and the aggregation of the generated metal oxides during the calcination process [51,52]. Additionally, the SEM images of Con-$MnFe_{0.6}Co_{0.4}O_x$ presented in Fig. S10 clearly show that it did not have any macropores. Due to the special hierarchically ordered structure of Hierc-$MnFe_{0.6}Co_{0.4}O_x$, the soot particulates can reach to the macropores, and they had a good connection with the active sites, ultimately leading to clearly enhanced soot resistance performance.

Transmission electron microscopy (TEM) was performed to examine the morphology and structure of a typical sample (Hierc-$MnFe_{0.6}Co_{0.4}O_x$; Fig. 4a–b). It is evident from the TEM image that the Hierc-$MnFe_{0.6}Co_{0.4}O_x$ catalyst has a uniform high quality hierarchically ordered structure, which is consistent with the SEM analysis. The high angle annular dark-field scanning TEM (HAADF-STEM) image and the corresponding elemental energy-dispersive X-ray spectroscopy (EDS) mapping images of the Hierc-$MnFe_{0.6}Co_{0.4}O_x$ catalyst presented in Fig. 4c–f indicated that Mn, Fe and Co were uniformly dispersed in the hierarchically ordered catalyst.

3.3. Crystal and textural structure of catalysts

X-ray diffraction (XRD) patterns of the as-prepared catalysts are displayed in Fig. 5 and Fig. S11. All the Bragg diffraction peaks in the 2θ range of 10°–80° could be well indexed. The pure Hierc-FeO_x showed a typical hexagonal crystalline structure (PDF#33-0664), while Hierc-CoO_x showed a cubic Co_3O_4 crystalline structure (PDF#43-1003). For pure Hierc-MnO_x, two crystal phases, namely Mn_3O_4 and Mn_2O_3, could be observed. Regarding the Hierc-$MnFeO_x$ catalyst, both the Fe_2O_3 and Mn_2O_3 crystal phases could be detected. However, in addition to a normal Mn_3O_4 crystal phase, a special crystal phase, specifically $CoFe_2O_4$, was found in Hierc-$MnFe_{1-\delta}Co_\delta O_x$ ($\delta = 0.2, 0.4$ and 0.6) catalysts. This means that a strong interaction occurred in Co and Fe species, which might be one of the reasons for the enhanced activity after cobalt was added into $MnFeO_x$ oxides.

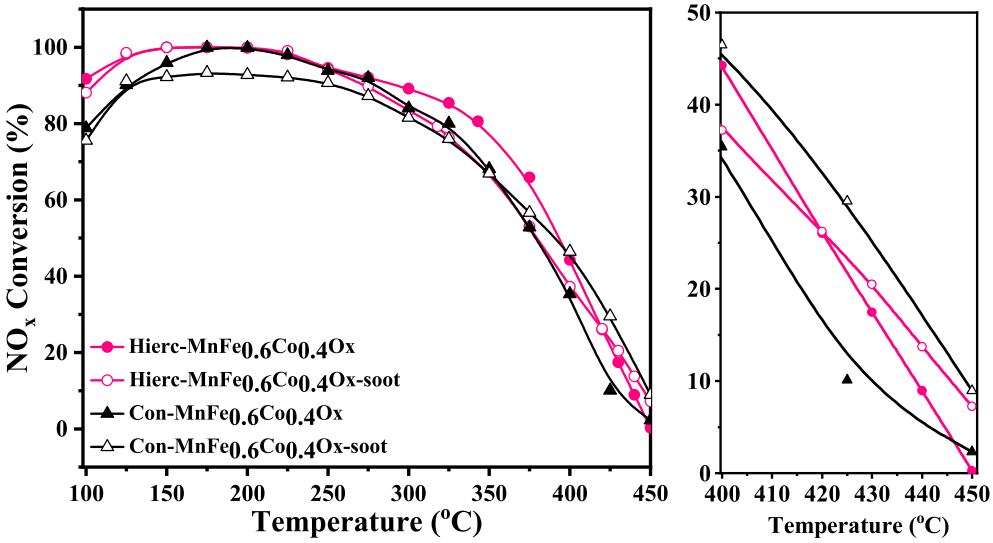

Fig. 2. Soot tolerance over Hierc-$MnFe_{0.6}Co_{0.4}O_x$ and Con-$MnFe_{0.6}Co_{0.4}O_x$ catalysts.

The textural properties are one of the main factors affecting the catalytic activity. Thus, the textural properties were measured by the N_2 adsorption/desorption technique. As shown in Fig. 6A, all the catalysts exhibited a typical type IV isotherm with an H3 hysteresis loop, indicating the formation of mesopores [53], and the average mesopore sizes estimated according to the BJH pore sizes of the samples (Fig. 6B) were in the range 8–11 nm. The specific surface area, pore volume, and pore diameter are listed in Table S2. The specific surface area of Hierc-$MnFe_{1-\delta}Co_\delta O_x$ catalysts (δ = 0.2, 0.4 and 0.6) is lower than that of monometal oxides, implying that their surface area was not the decisive effect on activity.

3.4. X-ray photoelectron spectroscopy of catalysts

XPS analysis was performed to determine the surface composition and valence state of the metal species. The Mn 2p, Fe 2p, Co 2p and O 1s spectra are displayed in Fig. 7. For Fe-containing catalysts, the main peak, corresponding to Fe $2p_{3/2}$ (~711 eV), can be fitted into two characteristic peaks, namely the peaks located at binding energies (BEs) of 710.6 and 712.7 eV, which could be assigned to Fe^{2+} and Fe^{3+}, respectively [54]. It has been reported that Fe^{3+} species have better catalytic performance than Fe^{2+} species, which is advantageous for adsorbing NH_3 and promoting the reduction of NO_x [55]. Based on the data in Table S3, it could be concluded that the Fe^{3+} ratio increased after cobalt was doped into Hierc-$MnFeO_x$. Using the peak-fitting deconvolution technique, the Mn $2p_{3/2}$ spectra located at BE ~ 642 eV could be fitted into three characteristic peaks, specifically at BE ~ 640.7, 642.2 and 643.9 eV, which are ascribed to Mn^{2+}, Mn^{3+} and Mn^{4+}, respectively [25]. Additionally, the Co 2p spectra of six Co-containing catalysts are shown. The peak of Co $2p_{3/2}$ at a BE of ~781 eV could be separated into two peaks (780.5 and 781.8 eV), which are assigned to the Co^{3+} and Co^{2+} species, respectively [56]. According to the data in Table S3, the atomic proportion of Mn^{4+}/Mn_{total} in Hierc-$MnFe_{0.6}Co_{0.4}O_x$ is 32%, which is much higher than that in Hierc-$MnFeO_x$ (20%). It is widely established that the abundant Mn^{4+} species are advantageous to the low-temperature redox ability on Mn-based catalysts. Mn^{4+} ions usually play an irreplaceable part in the oxidation of NO, which could enhance the low-temperature NH_3 SCR performance via the "fast SCR" process on the basis of the general reaction shown in Eq.(8) [57,58]. Moreover, Hierc-$MnFe_{0.6}Co_{0.4}O_x$ had a higher ratio of Co^{3+}/Co than Hierc-$MnFe_{0.8}Co_{0.2}O_x$ and Hierc-$MnFe_{0.4}Co_{0.6}O_x$, and the main forms of Co were different, Co mainly existed in the form Co^{2+} ($CoFe_2O_4$) in the bulk based on XRD results; however, it mainly existed in the form with +3 valence on the surface of the catalyst. According to the above results, it is reasonable to assume that Co^{3+} species play a key role in the improvement of the *de*NO_x performance, as they could bring excess surface oxygen and enhance gas molecular adsorption [59,60]. The O 1s spectra of all the catalysts can be divided into two different O species, namely O_α and O_β. Based on previous studies, the peaks at the low BE of ~530 eV (O_β) and high BE of ~532 eV (O_α) were assigned to the lattice oxygen and the surface-active oxygen species, respectively [61,62]. The ratio of $O_\alpha/(O_\alpha + O_\beta)$ increased after cobalt was added into Hierc-$MnFeO_x$, which was obtained from the peak areas and the proportions of O_α and O_β. It is generally accepted that the surface-active O species are more beneficial than the lattice O species. The existence of more surface-adsorbed active oxygen species was beneficial to oxidation of NO to NO_2 and adsorption of NH_3 due to its high mobility [63]. Common knowledge holds that the adsorption of NH_3 is the first process in the *de*NO_x reaction. Ultimately, the improvement of NO oxidation and NH_3 adsorption over Hierc-$MnFe_{1-\delta}Co_\delta O_x$ catalysts should be one of the main reasons for the increase of the catalytic activity. Based on the above results, a redox cycle for the NH_3-SCR reaction at low temperatures over the novel Hierc-$MnFe_{1-\delta}Co_\delta O_x$ catalysts can be proposed, as shown in Fig. 8 (where M and N represent two different metal elements). During the NH_3-SCR reaction, O_2 can obtain an electron from M^{n+} (where M^{n+}represents Fe^{2+}, Co^{2+}, Mn^{2+} and Mn^{3+}) to form O^- and $M^{(n+1)+}$. Also, NO can transfer an electron to $M^{(n+1)+}$ to form NO^+ and M^{n+}. The activation of NO and O_2 might be expressed as shown in Eqs. (11) and (12)

$$\frac{1}{2}O_2 + M^{n+} \rightarrow O^-_{ads} + M^{(n+1)+}, \quad (11)$$

$$NO + M^{(n+1)+} \rightarrow M^{n+} + NO^+_{ads}, \quad (12)$$

and NO_2 is formed as depicted in Eq. (13) [17,22]

$$O^-_{ads} + NO^+_{ads} \rightarrow NO_2. \quad (13)$$

3.5. H_2 temperature-programmed reduction and NH_3 temperature-programmed desorption analysis of catalysts

To investigate the reducibility of Hierc-$MnFe_{0.6}Co_{0.4}O_x$ and related catalysts, temperature-programmed reduction by hydrogen (H_2-TPR) tests were performed, as shown in Fig. 9a. According

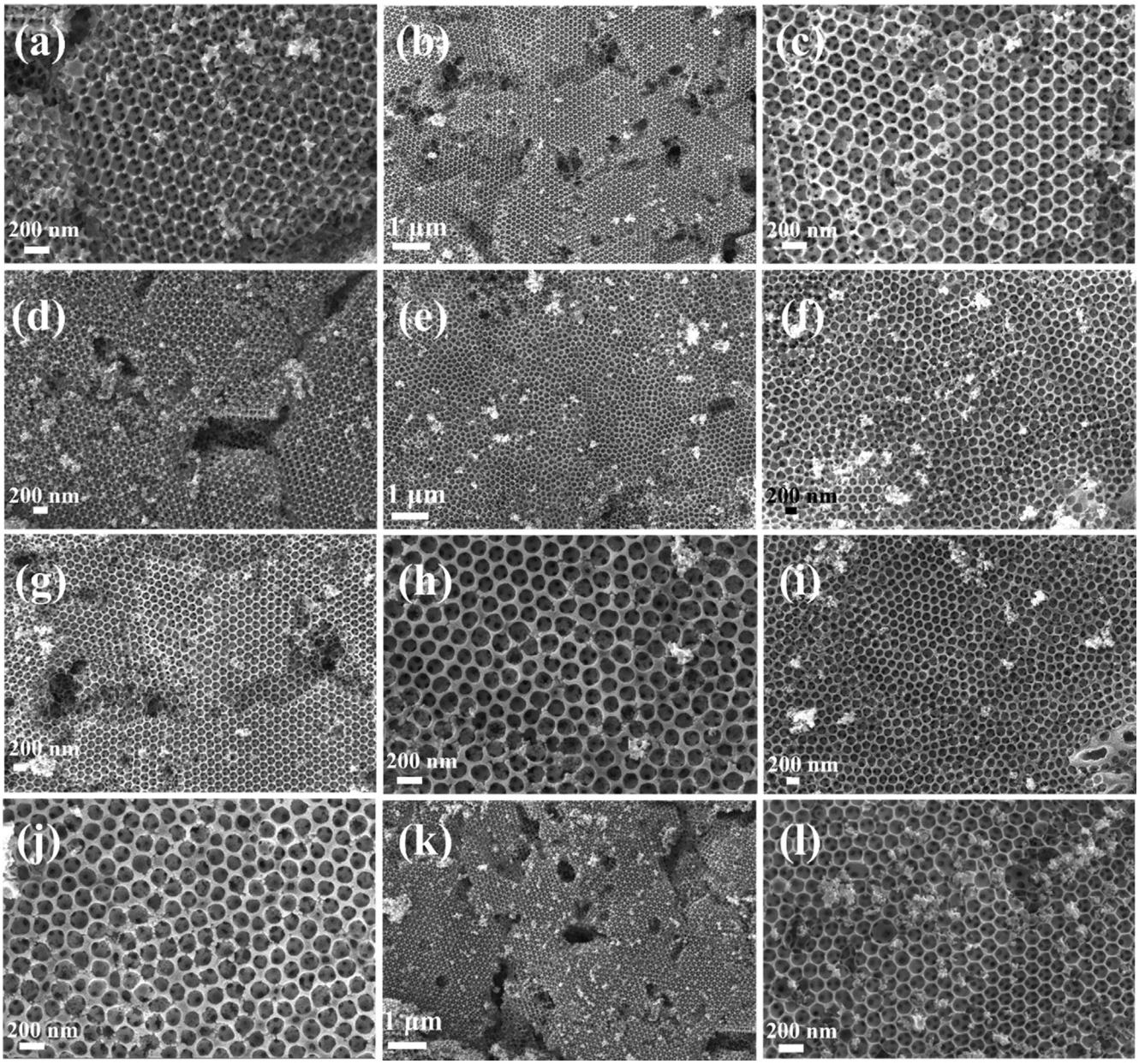

Fig. 3. SEM images of Hierc-$MnFe_{0.8}Co_{0.2}O_x$ (a), Hierc-$MnFe_{0.6}Co_{0.4}O_x$ (b, c), Hierc-$MnFe_{0.4}Co_{0.6}O_x$ (d), Hierc-$MnFeO_x$ (e, f), Hierc-FeO_x (g, h), Hierc-MnO_x (i, j), and Hierc-CoO_x (k, l).

to previous studies, the H_2 consumption peaks located at 200–300 °C are assigned to the reduction of $Fe^3 \rightarrow Fe^{(3-\delta)+}$, $Co^{3+} \rightarrow Co^{2+}$, $Mn^{4+} \rightarrow Mn^{3+}$ and $Mn^{3+} \rightarrow Mn^{2+}$, and the ones at 300–800 °C are ascribed to the reduction of $Co^{2+} \rightarrow Co^0$ and $Fe^{(3-\delta)+} \rightarrow Fe^0$ [64,65]. It is obvious that the reduction peak located at 585 °C shifted to the lower temperature (from 585 to 482 °C). According to this phenomenon, it can be inferred that the reduction capacity of FeO_x could be effectively promoted when cobalt was incorporated into Hierc-$MnFeO_x$, which accounted for the enhanced low-temperature activity over the Hierc-$MnFe_{0.6}Co_{0.4}O_x$ catalyst.

It is generally believed that NH_3 can be adsorbed and activated by the acid sites of the *de*NO_x catalysts. Thus, the acidity of Hierc-$MnFe_{0.6}Co_{0.4}O_x$ and related catalysts were investigated using temperature-programmed desorption of NH_3 (NH_3-TPD) (Fig. 9b). Based on earlier studies, the desorption peak below 200 °C can be ascribed to NH_3 adsorbed onto the weak acid sites, and the desorption peak between 200 and 500 °C can be attributed to the medium-strong acid sites [18]. It is obvious that the desorption peak areas of all the pure metal oxides catalysts were small, but the desorption peak area related to Hierc-$MnFe_{0.6}Co_{0.4}O_x$ was much larger than that of Hierc-$MnFeO_x$, especially the peak for medium-strong acid sites. Hierc-$MnFe_{0.6}Co_{0.4}O_x$ had the maximum acid amount. In general, the effect of adding Co on the acidic properties of the Hierc-$MnFeO_x$ catalyst was evident. The acid amount could increase after Co was doped into Hierc-$MnFeO_x$, which might promote NH_3 adsorption and ultimately resulted in better low-temperature NH_3-SCR performance.

3.6. In situ diffuse-reflectance infrared Fourier transform spectroscopy over Hierc-$MnFe_{0.6}Co_{0.4}O_x$ and Hierc-$MnFeO_x$ catalysts

3.6.1. Adsorption of NH_3 and co-adsorption of NO + O_2

To fully understand the effect of Co addition on the reaction mechanism, *in situ* diffuse reflectance infrared Fourier transform spectroscopy (DRIFTS) tests were conducted over the optimal sam-

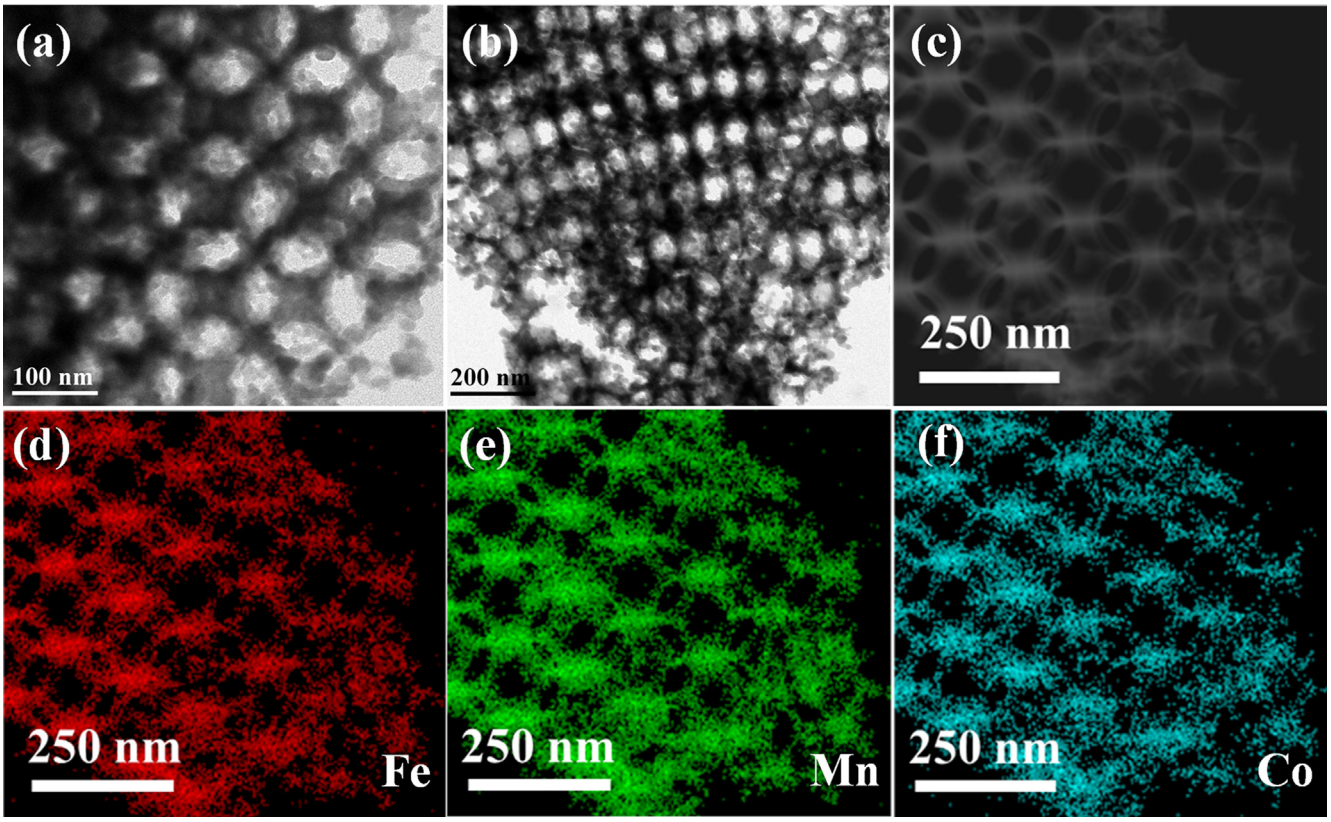

Fig. 4. TEM images (a, b), HAADF-STEM image (c), and elemental mapping images (d–f) of the Hierc-$MnFe_{0.6}Co_{0.4}O_x$ ternary metal oxide catalyst.

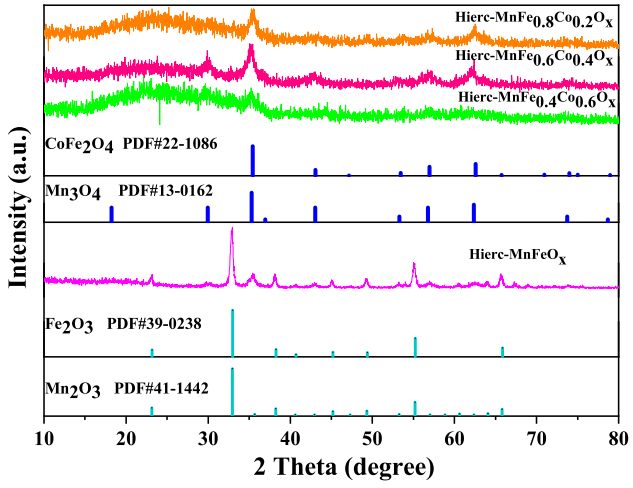

Fig. 5. XRD patterns of Hierc-$MnFe_{0.8}Co_{0.2}O_x$, Hierc-$MnFe_{0.6}Co_{0.4}O_x$, Hierc-$MnFe_{0.4}Co_{0.6}O_x$ and Hierc-$MnFeO_x$ catalysts.

ple (Hierc-$MnFe_{0.6}Co_{0.4}O_x$) and its counterpart sample (Hierc-$MnFeO_x$). Fig. S12 displays the *in situ* DRIFT spectra of NH_3 adsorption on Hierc-$MnFe_{0.6}Co_{0.4}O_x$ and Hierc-$MnFeO_x$ at 200 °C. As shown in Fig. S12 A, two weak bands related to coordinated NH_3 species (1302 cm^{-1}) and NH_3 coordinated with Lewis acid sites (1560 cm^{-1}, NH_3-L) could be observed in 11 min, and the band intensity slowly increased with treatment time. [66]. As for the typical Hierc-$MnFe_{0.6}Co_{0.4}O_x$ catalyst (Fig. S12B), it was found that more surface acid sites existed than on Hierc-$MnFeO_x$, the stronger band assigned to the NH_4^+ bounded to Brønsted acid sites (NH_4^+-B, 1402 cm^{-1}) could be detected in 5 min [67]. In addition, a band at 1538 cm^{-1} attributed to $-NH_2$ species appeared [30], suggesting that Hierc-$MnFe_{0.6}Co_{0.4}O_x$ has stronger oxidation performance than Hierc-$MnFeO_x$ and a better NH_3 activation process occurred on the surface of the Hierc-$MnFe_{0.6}Co_{0.4}O_x$. The relationship between the absorption band area and time is presented in Fig. S12E (the areas are the sum of all the absorption band marked in the figure). Compared with Fig. S12A, the absorption band area shown in Fig. S12B was bigger, implying that the surface of Hierc-$MnFe_{0.6}Co_{0.4}O_x$ could absorb more NH_3 species than that of Hierc-$MnFeO_x$, in accordance with the results of NH_3-TPD.

The co-adsorption of NO + O_2 over the Hierc-$MnFeO_x$ and Hierc-$MnFe_{0.6}Co_{0.4}O_x$ catalysts are shown in Figs. S12C and S12D. For the Hierc-$MnFeO_x$ catalyst, as presented in Fig. S12C, the bands at 1545 cm^{-1} can be ascribed to monodentate nitrate [16], and the band at 1234 cm^{-1} can be assigned to bridging nitrate [17]. After the proper amount of Co was doped, as depicted in Fig. S12D, the bands located at 1581 and 1290 cm^{-1} could be assigned respectively to bidentate nitrate and monodentate nitrate [65,68]. It is worth noting that the adsorption peak intensity of Hierc-$MnFe_{0.6}Co_{0.4}O_x$ was much higher than that of Hierc-$MnFeO_x$, which suggested that the Hierc-$MnFe_{0.6}Co_{0.4}O_x$ catalyst has better adsorption ability for NO species than Hierc-$MnFeO_x$ catalyst. Previous studies have confirmed that adsorbed NO_x-species plays a significant role not only in the reaction with NH_3 (thus giving rise to N_2 formation) but also in promoting the rate of the reoxidation step of the catalyst redox cycle [69–74]. Summarizing the above results, we can infer that the doping of Co species could effectively promote the adsorption behavior of NH_3 and NO_x species on the surface of Hierc-$MnFe_{0.6}Co_{0.4}O_x$, which might be in favor of the NH_3-SCR reaction at low temperature.

3.6.2. Reaction between flue gas NO + O_2 and preadsorbed NH_3 species

To study the *de*NO_x mechanism of the Hierc-$MnFe_{0.6}Co_{0.4}O_x$ catalyst, a series of *in situ* DRIFTS tests were conducted to investigate

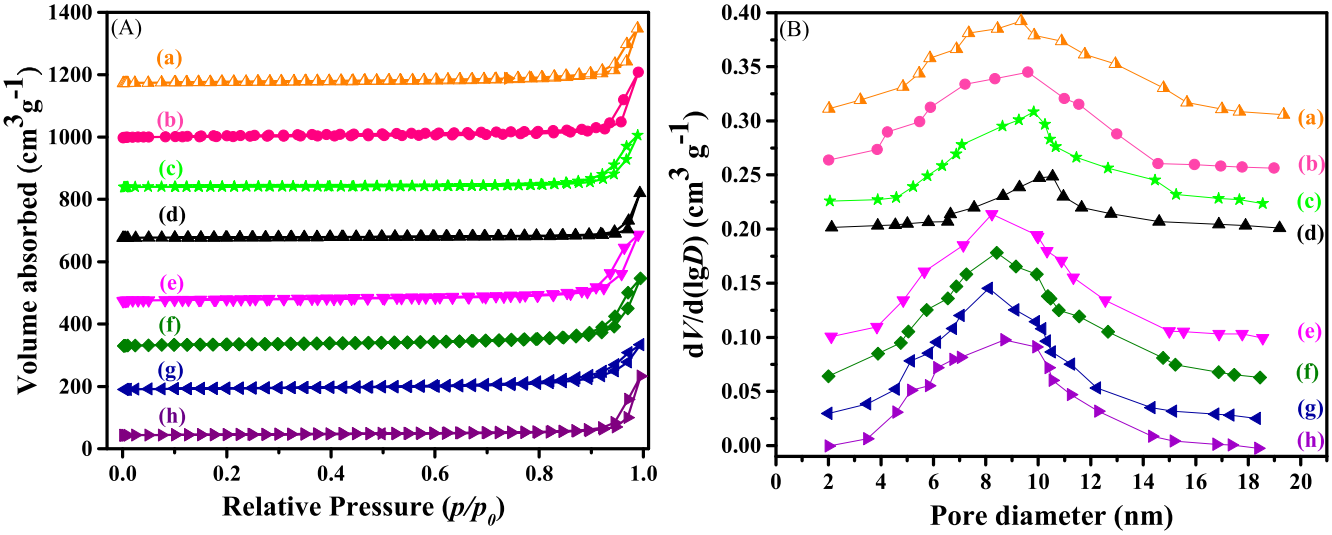

Fig. 6. (A) N_2 adsorption/desorption isotherms and (B) pore-size distributions of (a) Hierc-$MnFe_{0.8}Co_{0.2}O_x$, (b) Hierc-$MnFe_{0.6}Co_{0.4}O_x$, (c) Hierc-$MnFe_{0.4}Co_{0.6}O_x$, (d) Con-$MnFe_{0.6}Co_{0.4}O_x$, (e) Hierc-$MnFeO_x$, (f) Hierc-FeO_x, (g) Hierc-MnO_x, and (h) Hierc-CoO_x.

the adsorption and reaction behavior of the reactants and identify the crucial intermediates. First, the reaction between the pread-sorbed NH_3 species and the flue gases (NO + O_2) over the Hierc-$MnFe_{0.6}Co_{0.4}O_x$ catalyst was studied at 200 °C. As shown in Fig. 10, compared with Fig. S12B, some bands (such as 1402 cm^{-1}) vanished due to their weak adsorption stability, but

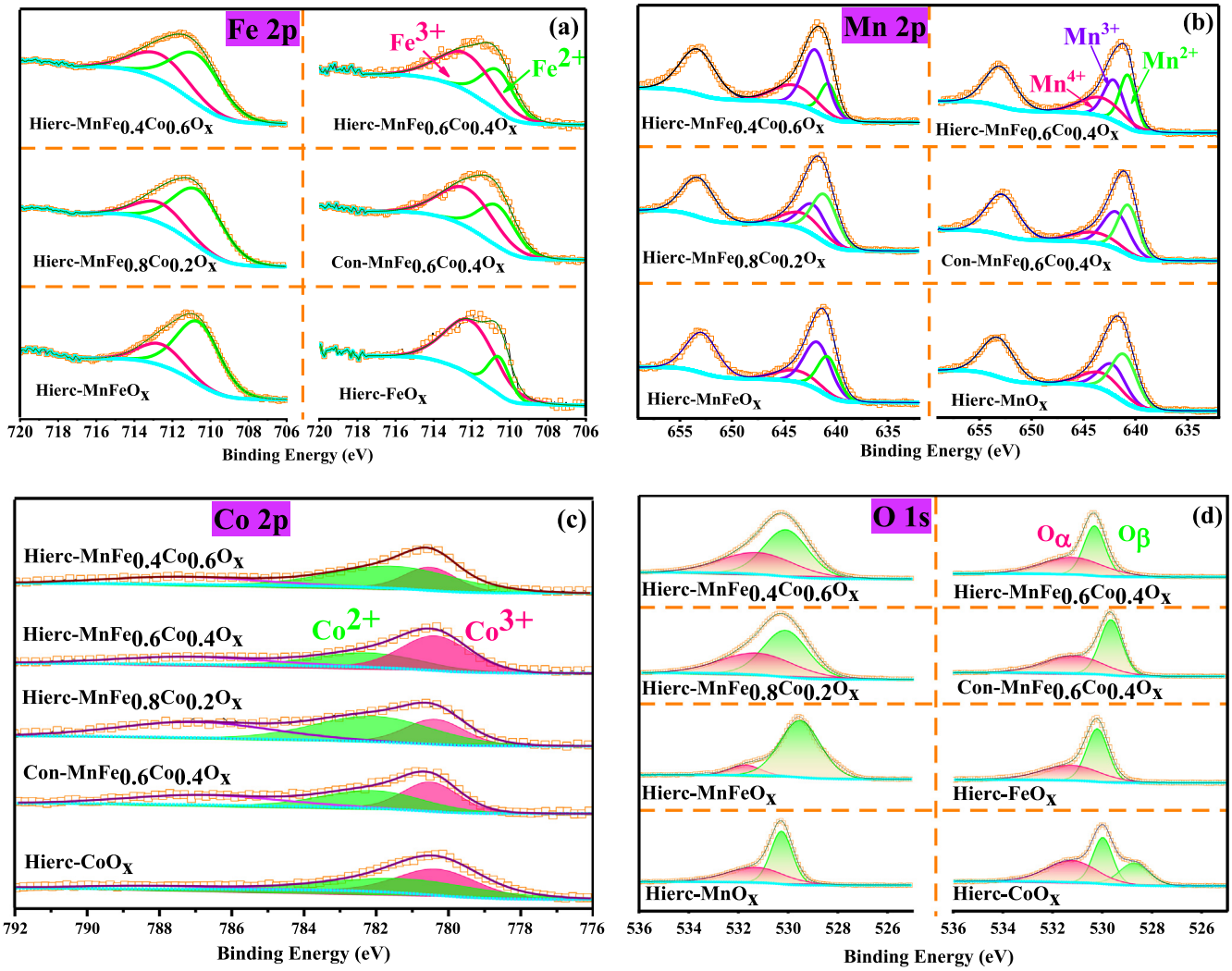

Fig. 7. XPS spectra of (a) Fe 2p, (b) Mn 2p, (c) Co 2p, and (d) O 1s over Hierc-$MnFe_{0.6}Co_{0.4}O_x$ and related catalysts.

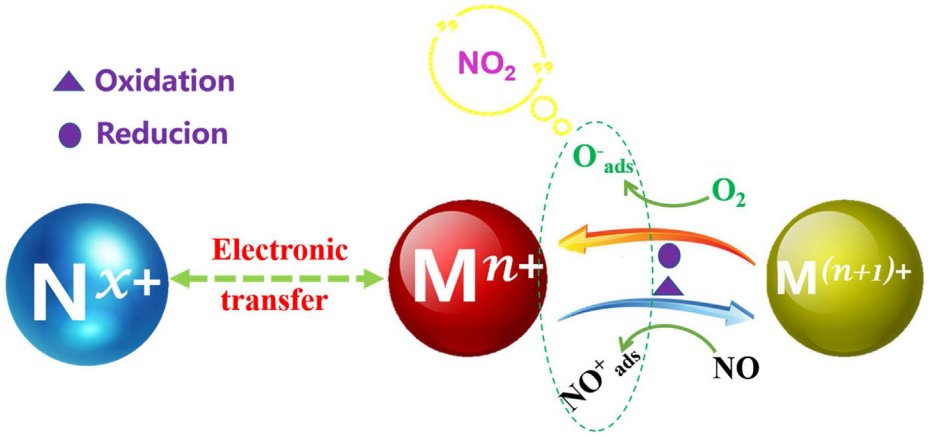

Fig. 8. Redox catalytic cycle of the low-temperature SCR reaction over Hierc-$MnFe_{1-\delta}Co_{\delta}O_x$ oxide catalysts.

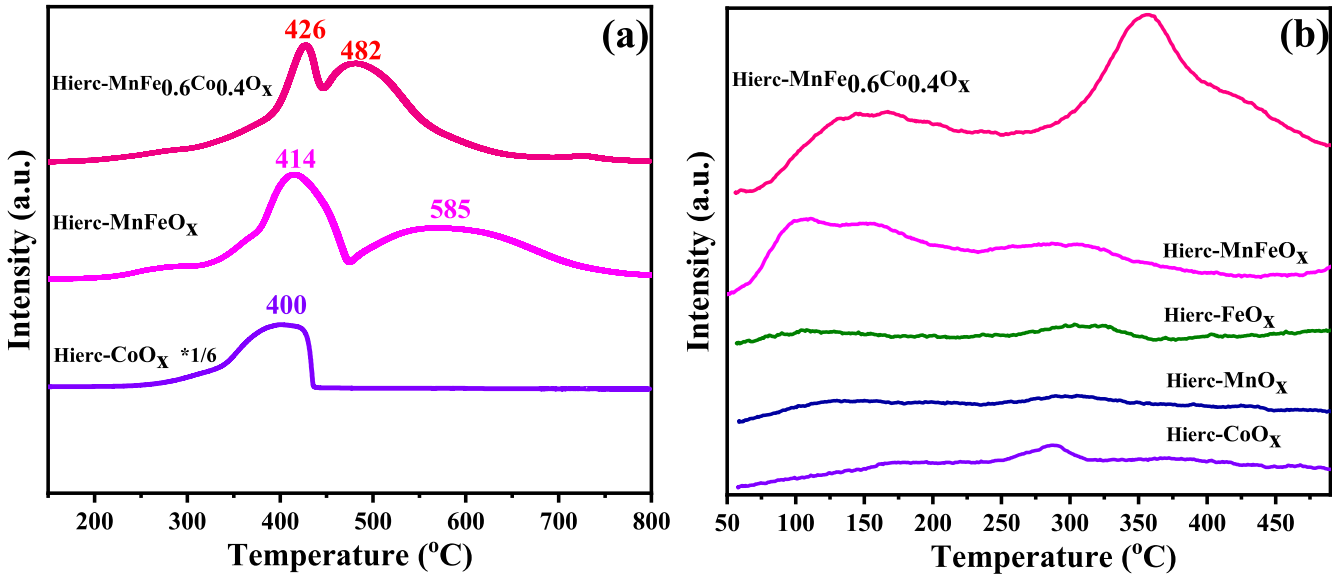

Fig. 9. H_2-TPR (a) and NH_3-TPD (b) profiles of Hierc-$MnFe_{0.6}Co_{0.4}O_x$ and related catalysts.

more new bands emerged when the pretreatment time was prolonged. The bands appearing at 1201 and 1611 cm^{-1} were detected in the spectrum of the Hierc-$MnFe_{0.6}Co_{0.4}O_x$ surface after 1 h of NH_3 adsorption, which were ascribed to NH_3 coordinated with Lewis acid sites (NH_3-L) [56,68]; the bands at 1695 and 1643 cm^{-1} could be attributed to the symmetric adsorption of the NH_3 bond at the Brønsted acid sites [18,75]. Then, following the introduction of flue gas (NO + O_2), after N_2 purging, the bands at 1695, 1643, and 1611 cm^{-1} disappeared immediately. However, the band intensity at 1201 cm^{-1} decreased and vanished completely 15 min later, and some new bands, corresponding to bidentate nitrates (1005 cm^{-1}) [49], monodentate nitrate species (1294 and 1459 cm^{-1}) [66,76], and bridging nitrate (1576 cm^{-1}) appeared in 20 min and the band intensity increased steadily due to the accumulation of the reaction products [66], which suggested that NH_3 could be adsorbed and activated by the acid sites and engaged in the reaction with nitrate species, indicating that the *de*NO_x reaction over Hierc-$MnFe_{0.6}Co_{0.4}O_x$ might follow the Langmuir–Hinshelwood (L–H) mechanism.

3.6.3. Reaction between flue gas NH_3 and preadsorbed NO + O_2 species

The DRIFTS spectra of Hierc-$MnFe_{0.6}Co_{0.4}O_x$ in a flue of NH_3 after being pre-exposed to an NO + O_2 atmosphere and then purged with N_2 at 200 °C are displayed in Fig. 11a. Exposure of Hierc-$MnFe_{0.6}Co_{0.4}O_x$ to NO + O_2 for 1 h resulted in the appearance of bands ascribed to monodentate nitrate (1299 cm^{-1}) [66], linear nitrites (1482 cm^{-1}), and bidentate nitrate (1581 cm^{-1}) [49,65]. After the flue gas NH_3 was introduced into the IR cell, the intensity of the IR bands assigned to the N-containing species was gradually reduced. Moreover, with increasing reaction time, the band at 1482 cm^{-1} shifted to 1472 cm^{-1}, and no bands of NH_3 species were observed in the spectrum. This might be because the adsorbed NH_3 was covered by the large number of adsorbed NO_x species, which implied that, similarly, the L–H mechanism might have occurred.

The above findings suggested that NH_3-SCR over the Hierc-$MnFe_{0.6}Co_{0.4}O_x$ catalyst might follow the L–H mechanism, according to the following equations (where * represents surface active sites):

$$O_2(g) + 2* \rightarrow 2O - *, \quad (14)$$

$$NH_3(g) + * \rightarrow NH_3 - *\text{coordinated } NH_3,\ NH_3 - L,\ NH_4 + -B, \quad (15)$$

$$NH_3 - * + O - * \rightarrow * - NH_2 + * - OH, \quad (16)$$

$$NO(g) + O - * \rightarrow * - NO_2 \text{ monodentate nitrate, linear nitrites, bridging nitrates,} \quad (17)$$

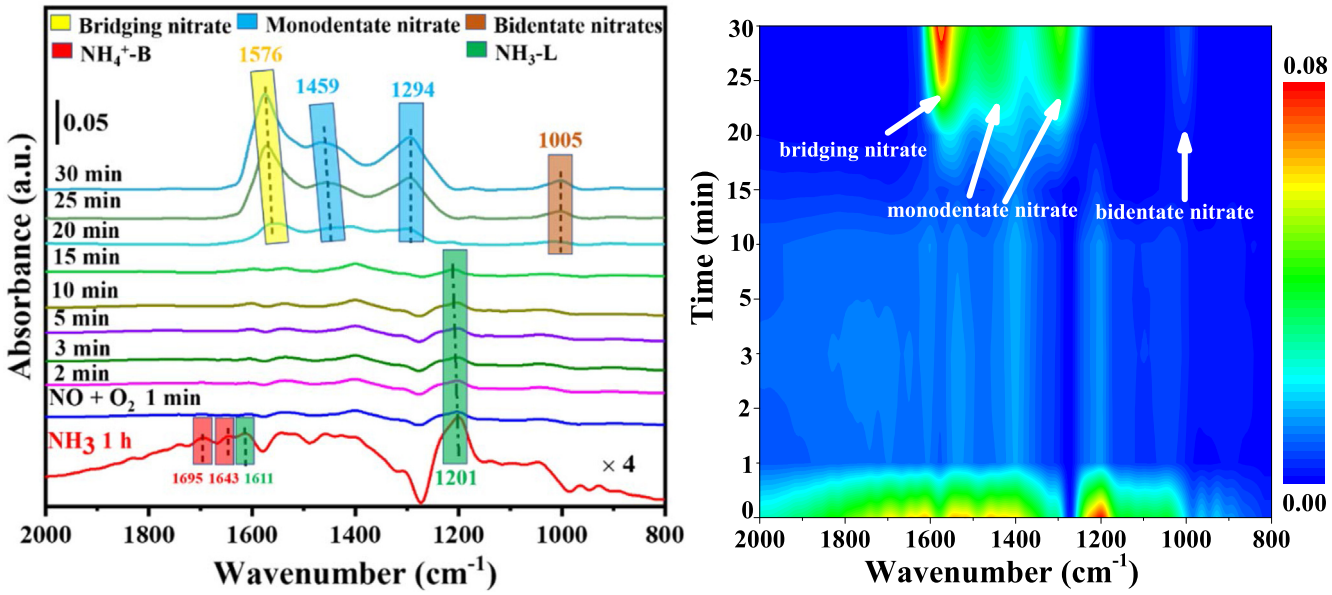

Fig. 10. In situ DRIFTS spectra of reaction between flue gases (NO + O_2) and the preadsorbed NH_3 at 200 °C and the corresponding mapping results (right) over the Hierc-$MnFe_{0.6}Co_{0.4}O_x$ catalyst.

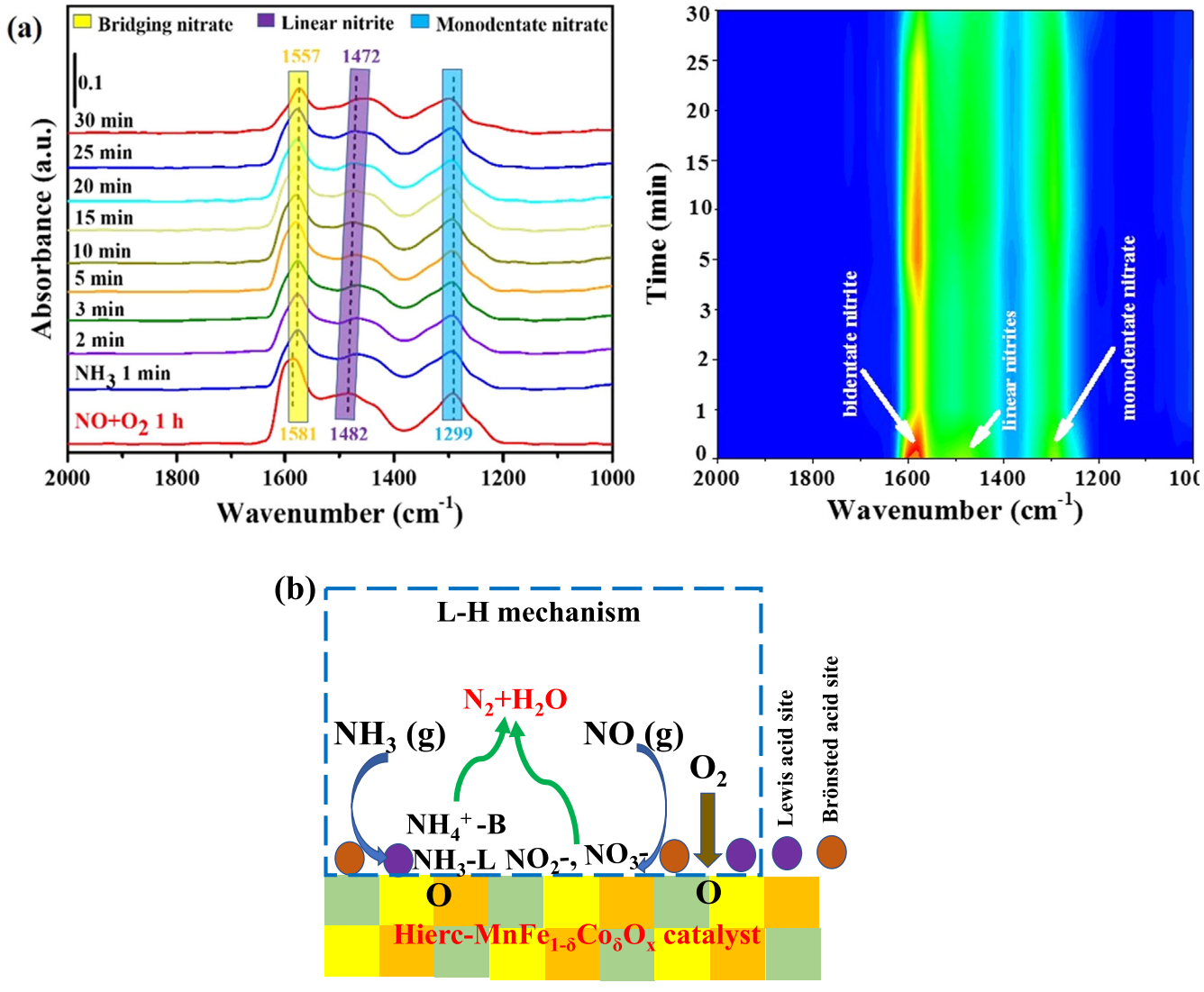

Fig. 11. (a) In situ DRIFTS spectra of reaction between NH_3 and preadsorbed NO + O_2 at 200 °C and the corresponding mapping results (right) over Hierc-$MnFe_{0.6}Co_{0.4}O_x$; (b) proposed NH_3-SCR reaction mechanism over Hierc-$MnFe_{0.6}Co_{0.4}O_x$.

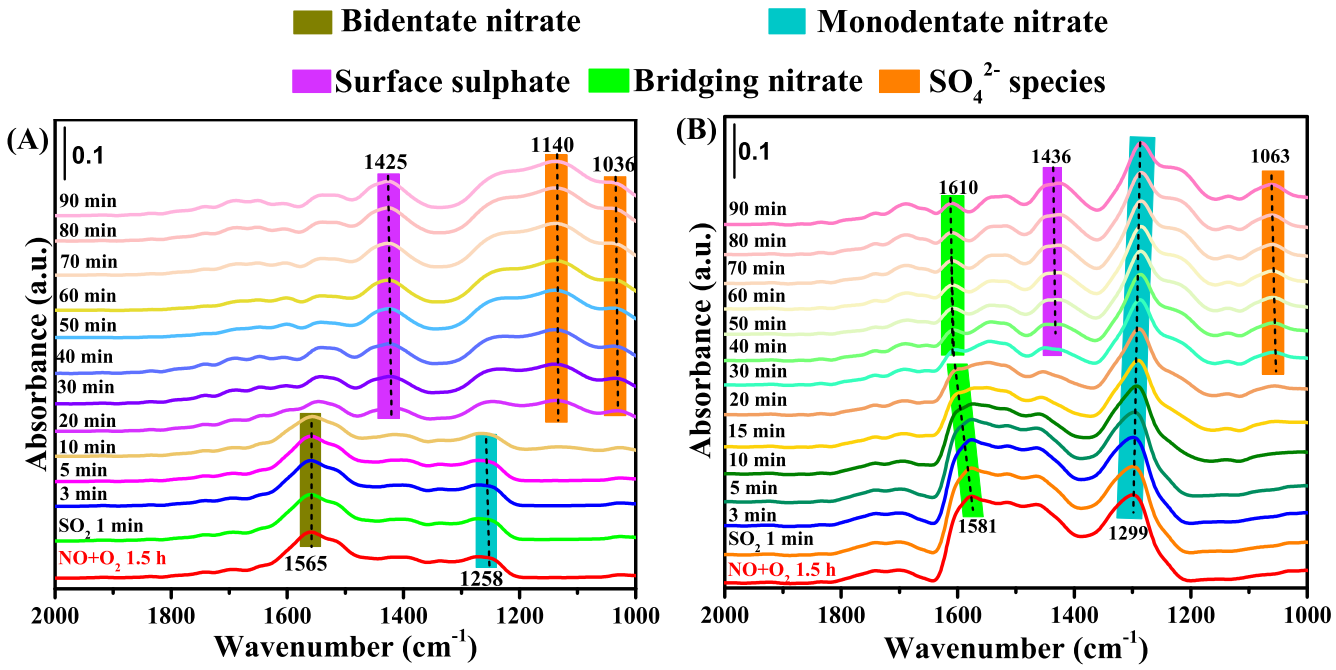

Fig. 12. In situ DRIFTS spectra of the influence of SO_2 on preadsorbed NO + O_2 over the (A) Hierc-$MnFeO_x$ and (B) Hierc-$MnFe_{0.6}Co_{0.4}O_x$ catalysts at 120 °C.

$$* - NH_2 + * - NO_2 \rightarrow N_2 + H_2O + O - * + *L - H \text{ mechanism.} \quad (18)$$

A schematic diagram of the proposed reaction mechanism is depicted in Fig. 11b.

3.6.4. Reaction between SO_2 + O_2 and the preadsorbed NO + O_2

To determine the reason for the better SO_2 tolerance performance of Hierc-$MnFe_{0.6}Co_{0.4}O_x$ at low temperature than that of Hierc-$MnFeO_x$, *in situ* DRIFTS analyses were conducted. As portrayed in Fig. 12, NO + O_2 species were preadsorbed on Hierc-$MnFe_{0.6}Co_{0.4}O_x$ and Hierc-$MnFeO_x$ for 1.5 h, then the flue gas (SO_2 + O_2) was introduced at 120 °C. For the Hierc-$MnFeO_x$ catalyst (Fig. 12A), the spectrum revealed adsorption peaks at 1565 and 1258 cm^{-1}, which have been attributed to bidentate nitrates and monodentate nitrate species [77], respectively. About 10 min later, these nitrate species almost vanished completely, and some new bands appeared at 1425, 1140 and 1036 cm^{-1}. The band centered at 1425 cm^{-1} is assigned to the surface sulfate species [78]. The peaks at 1140 and 1036 cm^{-1} correspond to the SO_4^{2-} species [79]. The trapping reaction can be represented as

$$SO_2(g) + O^* \rightarrow SO_3(ads), \quad (19)$$

$$SO_2(g) + M - O \rightarrow M - SO_3, \quad (20)$$

$$SO_3(ads) + M - O \rightarrow M - SO_4. \quad (21)$$

The aforementioned findings indicated that abundant sulfate species were formed on the Hierc-$MnFeO_x$ catalyst within sites exposed to SO_2 for 90 min, which led to the deactivation of the catalyst. However, for the Hierc-$MnFe_{0.6}Co_{0.4}O_x$ catalyst (Fig. 12B), the phenomenon showed some differences, and although sulfate species (1436 and 1063 cm^{-1}) could also be detected on the Hierc-$MnFe_{0.6}Co_{0.4}O_x$ catalyst [17,79], bridging nitrate (1581 and 1610 cm^{-1}) and monodentate nitrate (1299 cm^{-1}) always existed throughout the reaction [65,66,78], thus, these residual nitrate species could continue to participate in subsequent NH_3-SCR reactions. Importantly, the bridged nitrite, as a key transition state of the NO species, could still be present on the surface of the Hierc-$MnFe_{0.6}Co_{0.4}O_x$ catalyst during the reaction, due to its low stability, the formation, transformation, and decomposition of bridged nitrite accelerates the SCR reaction at low temperature [23,80]. These results suggested that the doping of Co could efficiently protect nitrate species from the poisoning effect of SO_2. As a result, the activity of the Hierc-$MnFe_{0.6}Co_{0.4}O_x$ catalyst could be maintained for a relatively longer time when exposed to SO_2, which could be attributed to the synergistic effect of the Co modification.

4. Conclusions

In summary, Co-doped $MnFeO_x$ ternary oxides with a hierarchically ordered structure (Hierc-$MnFe_{1-\delta}Co_\delta O_x$, δ = 0.2, 0.4 and 0.6) were prepared via a simple hard-template method. The Hierc-$MnFe_{1-\delta}Co_\delta O_x$ catalysts displayed boosted low-temperature activity for selective catalytic reduction of NO_x with NH_3. The NO_x conversion exceeded 80% between 90 and 343 °C and the active temperature window was evidently broadened over the Hierc-$MnFe_{0.6}Co_{0.4}O_x$ catalyst. After analysis by various techniques, the superior performance of NH_3-SCR reaction on the Co-modified Hierc-$MnFeO_x$ could be attributed to the larger number of active oxygen species and the higher ratios of Mn^{4+}, Fe^{3+} and Co^{3+} content, as well as the improvement of the surface acidity. Additionally, the Hierc-$MnFe_{0.6}Co_{0.4}O_x$ catalyst exhibited better soot tolerance due to its special hierarchically ordered architecture. Most importantly, Hierc-$MnFe_{0.6}Co_{0.4}O_x$ displayed remarkable SO_2 tolerance compared with the unmodified Hierc-$MnFeO_x$ catalyst. The *in situ* DRIFTS confirmed that the L–H mechanism might occur in the reaction and the doping of Co species could effectively promote the adsorption behavior of NH_3 and NO_x species on the surface of Hierc-$MnFe_{0.6}Co_{0.4}O_x$, which might be in favor of the NH_3-SCR reaction at low temperature. Moreover, the addition of Co could efficiently protect nitrate species on the Hierc-$MnFe_{0.6}Co_{0.4}O_x$ from the poisoning effect of SO_2, which accounted for its better SO_2 tolerance. Therefore, the Hierc-$MnFe_{1-\delta}Co_\delta O_x$ ternary oxides developed in this work provide a guidance for researchers to design high performance Mn-based low-

temperature catalysts for NH_3-SCR of NO_x with enhanced H_2O, soot, and SO_2 tolerance.

Declaration of Competing Interest

The authors declare that they have no known competing financial interests or personal relationships that could have appeared to influence the work reported in this paper.

Acknowledgments

This work was supported by the National Key R&D Program of China (2016YFC0205900), the National Natural Science Foundation of China (21976078 and 21773106), the Natural Science Foundation of Jiangxi Province (20201BAB203024), the National Engineering Laboratory for Mobile Source Emission Control Technology (NELMS2020A05), and the Foundation of State Key Laboratory of High-efficiency Utilization of Coal & Green Chemical Engineering (Grant No. 2018-K04), all of which are gratefully acknowledged by the authors.

Appendix A. Supplementary material

Supplementary data to this article can be found online at https://doi.org/10.1016/j.jcat.2020.12.036.

References

[1] G.C. Dhal, S. Dey, D. Mohan, R. Prasad, Simultaneous abatement of diesel soot and NO_x emissions by effective catalysts at low temperature: An overview, Catal. Rev. 60 (2018) 437–496.
[2] G. He, Z. Lian, Y. Yu, Y. Yang, K. Liu, X. Shi, Z. Yan, W. Shan, H. He, Polymeric vanadyl species determine the low-temperature activity of V-based catalysts for the SCR of NO_x with NH_3, Sci. Adv. 4 (2018) u4637.
[3] A. Marberger, D. Ferri, M. Elsener, O. Kröcher, The significance of lewis acid sites for the selective catalytic reduction of nitric oxide on vanadium-based catalysts, Angew. Chem. Int. Ed. 55 (2016) 11989–11994.
[4] L. Han, S. Cai, M. Gao, J. Hasegawa, P. Wang, J. Zhang, L. Shi, D. Zhang, Selective catalytic reduction of NO_x with NH_3 by using novel catalysts: state of the art and future prospects, Chem. Rev. 119 (2019) 10916–10976.
[5] L. Han, M. Gao, C. Feng, L. Shi, D. Zhang, Fe_2O_3-CeO_2@Al_2O_3 nanoarrays on Al-mesh as SO_2-tolerant monolith catalysts for NO_x reduction by NH_3, Environ. Sci. Technol. 53 (2019) 5946–5956.
[6] Q. Xu, Z. Fang, Y. Chen, Y. Guo, Y. Guo, L. Wang, Y. Wang, J. Zhang, W. Zhan, Titania–Samarium–manganese composite oxide for the low-temperature selective catalytic reduction of NO with NH_3, Environ. Sci. Technol. 54 (2020) 2530–2538.
[7] N. Zhu, W. Shan, Z. Lian, Y. Zhang, K. Liu, H. He, A superior Fe-V-Ti catalyst with high activity and SO_2 resistance for the selective catalytic reduction of NO_x with NH_3, J. Hazard. Mater. 382 (2020) 120970.
[8] L. Chen, Q. Wang, X. Wang, Q. Cong, H. Ma, T. Guo, S. Li, W. Li, High-performance CeO_2/halloysite hierarchical catalysts with promotional redox property and acidity for the selective catalytic reduction of NO with NH_3, Chem. Eng. J. 390 (2020) 124251.
[9] C. Li, Z. Huang, X. Liu, J. Chen, W. Qu, X. Jiang, H. Wang, Z. Ma, X. Tang, Y. Chen, Rational design of alkali-resistant catalysts for selective NO reduction with NH_3, Chem. Commun. 55 (2019) 9853–9856.
[10] S. Ding, F. Liu, X. Shi, H. He, Promotional effect of Nb additive on the activity and hydrothermal stability for the selective catalytic reduction of NO with NH_3 over $CeZrO_x$ catalyst, Appl. Catal. B Environ. 180 (2016) 766–774.
[11] X. Zhao, L. Huang, H. Li, H. Hu, X. Hu, L. Shi, D. Zhang, Promotional effects of zirconium doped $CeVO_4$ for the low-temperature selective catalytic reduction of NO_x with NH_3, Appl. Catal. B Environ. 183 (2016) 269–281.
[12] L. Xu, C. Wang, H. Chang, Q. Wu, T. Zhang, J. Li, New Insight into SO_2 poisoning and regeneration of CeO_2-WO_3/TiO_2 and V_2O_5-WO_3/TiO_2 catalysts for low-temperature NH_3-SCR, Environ. Sci. Technol. 52 (2018) 7064–7071.
[13] J. Fan, P. Ning, Z. Song, X. Liu, L. Wang, J. Wang, H. Wang, K. Long, Q. Zhang, Mechanistic aspects of NH_3-SCR reaction over CeO_2/TiO_2-ZrO_2-SO_4^{2-} catalyst: In situ DRIFTS investigation, Chem. Eng. J. 334 (2018) 855–863.
[14] Z. Huang, X. Gu, W. Wen, P. Hu, M. Makkee, H. Lin, F. Kapteijn, X. Tang, A "Smart" hollandite $DeNO_x$ catalyst: self-protection against alkali poisoning, Angew. Chem. Int. Ed. 52 (2013) 660–664.
[15] Z. Fan, J. Shi, C. Gao, G. Gao, B. Wang, C. Niu, Rationally designed porous MnO_x-FeO_x nanoneedles for low-temperature selective catalytic reduction of NO_x by NH_3, Appl. Mater. Interfaces 9 (2017) 16117–16127.
[16] H. Wang, P. Ning, Y. Zhang, Y. Ma, J. Wang, L. Wang, Q. Zhang, Highly efficient WO_3-FeO_x catalysts synthesized using a novel solvent-free method for NH_3-SCR, J. Hazard. Mater. 121812 (2019).
[17] C. Sun, H. Liu, W. Chen, D. Chen, S. Yu, A. Liu, L. Dong, S. Feng, Insights into the Sm/Zr co-doping effects on N_2 selectivity and SO_2 resistance of a MnO_x-TiO_2 catalyst for the NH_3-SCR reaction, Chem. Eng. J. 347 (2018) 27–40.
[18] S. Ma, X. Zhao, Y. Li, T. Zhang, F. Yuan, X. Niu, Y. Zhu, Effect of W on the acidity and redox performance of the $Cu_{0.02}Fe_{0.2}W_aTiO_x$ (a = 0.01, 0.02, 0.03) catalysts for NH_3-SCR of NO, Appl. Catal. B Environ. 248 (2019) 226–238.
[19] D. Meng, W. Zhan, Y. Guo, Y. Guo, L. Wang, G. Lu, A highly effective catalyst of Sm-MnO_x for the NH_3-SCR of NO_x at low temperature: promotional role of Sm and its catalytic performance, ACS Catal. 5 (2015) 5973–5983.
[20] N. Fang, J. Guo, S. Shu, H. Luo, Y. Chu, J. Li, Enhancement of low-temperature activity and sulfur resistance of $Fe_{0.3}Mn_{0.5}Zr_{0.2}$ catalyst for NO removal by NH_3-SCR, Chem. Eng. J. 325 (2017) 114–123.
[21] L. Chen, F. Yuan, Z. Li, X. Niu, Y. Zhu, Synergistic effect between the redox property and acidity on enhancing the low temperature NH3-SCR activity for NO removal over the Co0.2CexMn0.8-xTi10 (x = 0–0.40) oxides catalysts, Chem. Eng. J. 354 (2018) 393–406.
[22] Q. Yan, S. Chen, C. Zhang, Q. Wang, B. Louis, Synthesis and catalytic performance of $Cu_1Mn_{0.5}Ti_{0.5}O_x$ mixed oxide as low-temperature NH_3-SCR catalyst with enhanced SO_2 resistance, Appl. Catal. B Environ. 238 (2018) 236–247.
[23] C. Liu, J. Shi, C. Gao, C. Niu, Manganese oxide-based catalysts for low-temperature selective catalytic reduction of NO_x with NH_3: A review, Appl. Catal. A-Gen. 522 (2016) 54–69.
[24] H. Xu, N. Yan, Z. Qu, W. Liu, J. Mei, W. Huang, S. Zhao, Gaseous heterogeneous catalytic reactions over Mn-based oxides for environmental applications: A critical review, Environ. Sci. Technol. 51 (2017) 8879–8892.
[25] C. Gao, B. Xiao, J. Shi, C. He, B. Wang, D. Ma, Y. Cheng, C. Niu, Comprehensive understanding the promoting effect of Dy-doping on $MnFeO_x$ nanowires for the low-temperature NH_3-SCR of NO_x: An experimental and theoretical study, J. Catal. 380 (2019) 55–67.
[26] H. Chang, J. Li, X. Chen, L. Ma, S. Yang, J.W. Schwank, J. Hao, Effect of Sn on MnO_x-CeO_2 catalyst for SCR of NO_x by ammonia: Enhancement of activity and remarkable resistance to SO_2, Catal. Commun. 27 (2012) 54–57.
[27] Z. Liu, J. Zhu, J. Li, L. Ma, S.I. Woo, Novel Mn-Ce-Ti mixed oxide catalyst for the selective catalytic reduction of NO_x with NH_3, ACS Appl. Mater. Interfaces 6 (2014) 14500–14508.
[28] J. Qiao, N. Wang, Z. Wang, W. Sun, K. Sun, Porous bimetallic $Mn_2Co_1O_x$ catalysts prepared by a one-step combustion method for the low temperature selective catalytic reduction of NO_x with NH_3, Catal. Commun. 72 (2015) 111–115.
[29] X. Tang, C. Li, H. Yi, L. Wang, Q. Yu, F. Gao, X. Cui, C. Chu, J. Li, R. Zhang, Facile and fast synthesis of novel Mn_2CoO_4@rGO catalysts for the NH_3-SCR of NO_x at low temperature, Chem. Eng. J. 333 (2018) 467–476.
[30] F. Wang, B. Shen, S. Zhu, Z. Wang, Promotion of Fe and Co doped Mn-Ce/TiO_2 catalysts for low temperature NH_3-SCR with SO_2 tolerance, Fuel 249 (2019) 54–60.
[31] J. Yu, F. Guo, Y. Wang, J. Zhu, Y. Liu, F. Su, S. Gao, G. Xu, Sulfur poisoning resistant mesoporous Mn-base catalyst for low-temperature SCR of NO with NH_3, Appl. Catal. B Environ. 95 (2010) 160–168.
[32] X. Wu, C. Wang, Y. Wei, J. Xiong, Y. Zhao, Z. Zhao, J. Liu, J. Li, Multifunctional photocatalysts of Pt-decorated 3DOM perovskite-type $SrTiO_3$ with enhanced CO_2 adsorption and photoelectron enrichment for selective CO_2 reduction with H_2O to CH_4, J. Catal. 377 (2019) 309–321.
[33] X. Yu, L. Wang, M. Chen, X. Fan, Z. Zhao, K. Cheng, Y. Chen, Z. Sojka, Y. Wei, J. Liu, Enhanced activity and sulfur resistance for soot combustion on three-dimensionally ordered macroporous-mesoporous $Mn_xCe_{1-x}O_\delta$/SiO_2 catalysts, Appl. Catal. B Environ. 254 (2019) 246–259.
[34] Y. Wei, J. Liu, Z. Zhao, Y. Chen, C. Xu, A. Duan, G. Jiang, H. He, Highly active catalysts of gold nanoparticles supported on three-dimensionally ordered macroporous $LaFeO_3$ for soot oxidation, Angew. Chem. Int. Ed. 50 (2011) 2326–2329.
[35] J. Zhao, Y. Shu, P. Zhang, Solid-state CTAB-assisted synthesis of mesoporous Fe_3O_4 and Au@Fe_3O_4 by mechanochemistry, Chin. J. Catal. 40 (2019) 1078–1084.
[36] Y. Wei, Z. Zhao, T. Li, J. Liu, A. Duan, G. Jiang, The novel catalysts of truncated polyhedron Pt nanoparticles supported on three-dimensionally ordered macroporous oxides (Mn, Fe Co, Ni, Cu) with nanoporous walls for soot combustion, Appl. Catal. B Environ. 146 (2014) 57–70.
[37] M.A.A. Aziz, A.A. Jalil, S. Triwahyono, R.R. Mukti, Y.H. Taufiq-Yap, M.R. Sazegar, Highly active Ni-promoted mesostructured silica nanoparticles for CO_2 methanation, Appl. Catal. B Environ. 147 (2014) 359–368.
[38] S.T. Oyama, X. Zhang, J. Lu, Y. Gu, T. Fujitani, Epoxidation of propylene with H_2 and O_2 in the explosive regime in a packed-bed catalytic membrane reactor, J. Catal. 257 (2008) 1–4.
[39] T. Wang, J. Xing, L. Zhu, A. Jia, Y. Wang, J. Lu, M. Luo, CO oxidation over supported Pt/$Cr_xFe_{2-x}O_3$ catalysts and their good tolerance to CO_2 and H_2O, Appl. Catal. B Environ. 245 (2019) 314–324.
[40] X. Wu, H. Meng, Y. Du, J. Liu, B. Hou, X. Xie, Insight into Cu_2O/CuO collaboration in the selective catalytic reduction of NO with NH_3: Enhanced activity and synergistic mechanism, J. Catal. 384 (2020) 72–87.
[41] B. Meng, Z. Zhao, X. Wang, J. Liang, J. Qiu, Selective catalytic reduction of nitrogen oxides by ammonia over Co_3O_4 nanocrystals with different shapes, Appl. Catal. B Environ. 129 (2013) 491–500.

[42] R. Ke, J. Li, X. Liang, J. Hao, Novel promoting effect of SO_2 on the selective catalytic reduction of NO_x by ammonia over Co_3O_4 catalyst, Catal. Commun. 8 (2007) 2096–2099.
[43] F. Liu, H. He, C. Zhang, Z. Feng, L. Zheng, Y. Xie, T. Hu, Selective catalytic reduction of NO with NH_3 over iron titanate catalyst: Catalytic performance and characterization, Appl. Catal. B Environ. 96 (2010) 408–420.
[44] L. Arnarson, H. Falsig, S.B. Rasmussen, J.V. Lauritsen, P.G. Moses, A complete reaction mechanism for standard and fast selective catalytic reduction of nitrogen oxides on low coverage $VO_x/TiO_2(001)$ catalysts, J. Catal. 346 (2017) 188–197.
[45] M. Koebel, G. Madia, F. Raimondi, A. Wokaun, Enhanced reoxidation of vanadia by NO_2 in the fast SCR reaction, J. Catal. 209 (2002) 159–165.
[46] M. Koebel, M. Elsener, G. Madia, Reaction pathways in the selective catalytic reduction process with NO and NO_2 at low temperatures, Ind. Eng. Chem. Res. 40 (2001) 52–59.
[47] J. Liu, X. Shi, Y. Shan, Z. Yan, W. Shan, Y. Yu, H. He, Hydrothermal stability of CeO_2-WO_3-ZrO_2 mixed oxides for selective catalytic reduction of NO_x by NH_3, Environ. Sci. Technol. 52 (2018) 11769–11777.
[48] H. Xu, Y. Li, B. Xu, Y. Cao, X. Feng, M. Sun, M. Gong, Y. Chen, Effectively promote catalytic performance by adjusting W/Fe molar ratio of $FeW_x/Ce_{0.68}Zr_{0.32}O_2$ monolithic catalyst for NH_3-SCR, J. Ind. Eng. Chem. 36 (2016) 334–345.
[49] X. Yao, L. Chen, J. Cao, Y. Chen, M. Tian, F. Yang, J. Sun, C. Tang, L. Dong, Enhancing the *de*NO_x performance of MnO_x/CeO_2-ZrO_2 nanorod catalyst for low-temperature NH_3-SCR by TiO_2 modification, Chem. Eng. J. 369 (2019) 46–56.
[50] J. Li, H. Chang, L. Ma, J. Hao, R.T. Yang, Low-temperature selective catalytic reduction of NO_x with NH_3 over metal oxide and zeolite catalysts-A review, Catal. Today 175 (2011) 147–156.
[51] B. Jin, Y. Wei, Z. Zhao, J. Liu, X. Yu, Y. Li, J. Li, Synthesis of three-dimensionally ordered macroporous Al-Ce mixed oxide catalysts with high catalytic activity and stability for diesel soot combustion, Catal. Today 258 (2015) 487–497.
[52] Y. Zhang, J. Deng, H. Zhang, Y. Liu, H. Dai, Three-dimensionally ordered macroporous Pr_6O_{11} and Tb_4O_7 with mesoporous walls: Preparation, characterization, and catalytic activity for CO oxidation, Catal. Today 245 (2015) 28–36.
[53] F. Yu, X. Xu, H. Peng, H. Yu, Y. Dai, W. Liu, J. Ying, Q. Sun, X. Wang, Porous NiO nano-sheet as an active and stable catalyst for CH_4 deep oxidation, Appl. Catal. A Gen. 507 (2015) 109–118.
[54] W. Niu, L. Li, X. Liu, N. Wang, J. Liu, W. Zhou, Z. Tang, S. Chen, Mesoporous N-doped carbons prepared with thermally removable nanoparticle templates: an efficient electrocatalyst for oxygen reduction reaction, J. Am. Chem. Soc. 137 (2015) 5555–5562.
[55] X. Zhou, X. Huang, A. Xie, S. Luo, C. Yao, X. Li, S. Zuo, V_2O_5-decorated Mn-Fe/attapulgite catalyst with high SO_2 tolerance for SCR of NO_x with NH_3 at low temperature, Chem. Eng. J. 326 (2017) 1074–1085.
[56] Z. Wang, R. Guo, X. Shi, X. Liu, H. Qin, Y. Liu, C. Duan, D. Guo, W. Pan, The superior performance of $CoMnO_x$ catalyst with ball-flowerlike structure for low-temperature selective catalytic reduction of NO_x by NH_3, Chem. Eng. J. 381 (2020) 122753.
[57] X. Tang, J. Li, L. Sun, J. Hao, Origination of N_2O from NO reduction by NH_3 over β-MnO_2 and α-Mn_2O_3, Appl. Catal. B Environ. 99 (2010) 156–162.
[58] S.S.R. Putluru, L. Schill, A.D. Jensen, B. Siret, F. Tabaries, R. Fehrmann, Mn/TiO_2 and $Mn-Fe/TiO_2$ catalysts synthesized by deposition precipitation-promising for selective catalytic reduction of NO with NH_3 at low temperatures, Appl. Catal. B Environ. 165 (2015) 628–635.
[59] B. Bai, H. Arandiyan, J. Li, Comparison of the performance for oxidation of formaldehyde on nano-Co_3O_4, 2D-Co_3O4, and 3D-Co_3O_4 catalysts, Appl. Catal. B Environ. 142–143 (2013) 677–683.
[60] H. Hu, S. Cai, H. Li, L. Huang, L. Shi, D. Zhang, Mechanistic aspects of deNO_x processing over TiO_2 supported Co-Mn oxide catalysts: structure-activity relationships and in situ DRIFTs analysis, ACS Catal. 5 (2015) 6069–6077.
[61] S. Yang, C. Wang, J. Li, N. Yan, L. Ma, H. Chang, Low temperature selective catalytic reduction of NO with NH_3 over Mn-Fe spinel: Performance, mechanism and kinetic study, Appl. Catal. B Environ. 110 (2011) 71–80.
[62] F. Wang, Z. Xie, J. Liang, B. Fang, Y.A. Piao, M. Hao, Z. Wang, Tourmaline-modified $FeMnTiO_x$ catalysts for improved low-temperature NH_3-SCR performance, Environ. Sci. Technol. 53 (2019) 6989–6996.
[63] S. Gillot, G. Tricot, H. Vezin, J. Dacquin, C. Dujardin, P. Granger, Induced effect of tungsten incorporation on the catalytic properties of $CeVO_4$ systems for the selective reduction of NO_x by ammonia, Appl. Catal. B Environ. 234 (2018) 318–328.
[64] R. Wang, Z. Hao, Y. Li, G. Liu, H. Zhang, H. Wang, Y. Xia, S. Zhan, Relationship between structure and performance of a novel highly dispersed MnO_x on Co-Al layered double oxide for low temperature NH_3-SCR, Appl. Catal. B Environ. 258 (2019) 117983.
[65] F. Liu, H. He, Structure-activity relationship of iron titanate catalysts in the selective catalytic reduction of NO_x with NH_3, J. Phys. Chem. C 114 (2010) 16929–16936.
[66] X. Li, J. Li, Y. Peng, H. Chang, T. Zhang, S. Zhao, W. Si, J. Hao, Mechanism of arsenic poisoning on SCR catalyst of CeW/Ti and its novel efficient regeneration method with hydrogen, Appl. Catal. B Environ. 184 (2016) 246–257.
[67] S. Zhan, H. Zhang, Y. Zhang, Q. Shi, Y. Li, X. Li, Efficient NH_3-SCR removal of NOx with highly ordered mesoporous $WO_3(\chi)$-CeO_2 at low temperatures, Appl. Catal. B Environ. 203 (2017) 199–209.
[68] L. Chen, J. Li, M. Ge, DRIFT study on cerium-tungsten/titiania catalyst for selective catalytic reduction of NO_x with NH_3, Environ. Sci. Technol. 44 (2010) 9590–9596.
[69] V. Vargheese, J. Murakami, K.K. Bando, I. Tyrone Ghampson, G. Yun, Y. Kobayashi, S. Ted Oyama, The direct molecular oxygen partial oxidation of CH_4 to dimethyl ether without methanol formation over a Pt/Y_2O_3 catalyst using an NO/NO_2 oxygen atom shuttle, J. Catal. 389 (2020) 352–365.
[70] M. Koebel, M. Elsener, M. Kleemann, Urea-SCR: a promising technique to reduce NO_x emissions from automotive diesel engines, Catal. Today 59 (2000) 335–345.
[71] A. Beretta, A. Lanza, L. Lietti, S. Alcove Clave, J. Collier, M. Nash, An investigation on the redox kinetics of NH_3-SCR over a V/Mo/Ti catalyst: Evidence of a direct role of NO in the re-oxidation step, Chem. Eng. J. 359 (2019) 88–98.
[72] I. Nova, C. Ciardelli, E. Tronconi, D. Chatterjee, B. Bandl Konrad, NH_3-SCR of NO over a V-based catalyst: Low-T redox kinetics with NH_3 inhibition, AIChE J. 52 (2006) 3222–3233.
[73] V. Vargheese, Y. Kobayashi, S.T. Oyama, The direct partial oxidation of methane to dimethyl ether over Pt/Y_2O_3 catalysts using an NO/O_2 shuttle, Angew. Chem. Int. Ed. 59 (2020) 16644–16650.
[74] G. Madia, M. Koebel, M. Elsener, A. Wokaun, The effect of an oxidation precatalyst on the NO_x reduction by ammonia SCR, Ind. Eng. Chem. Res. 41 (2002) 3512–3517.
[75] Z. Fan, J. Shi, C. Gao, G. Gao, B. Wang, Y. Wang, C. He, C. Niu, Gd-modified MnOx for the selective catalytic reduction of NO by NH_3: The promoting effect of Gd on the catalytic performance and sulfur resistance, Chem. Eng. J. 348 (2018) 820–830.
[76] J. Tan, Y. Wei, Y. Sun, J. Liu, Z. Zhao, W. Song, J. Li, X. Zhang, Simultaneous removal of NO_x and soot particulates from diesel engine exhaust by 3DOM Fe-Mn oxide catalysts, J. Ind. Eng. Chem. 63 (2018) 84–94.
[77] T.H. Vuong, J. Radnik, J. Rabeah, U. Bentrup, M. Schneider, H. Atia, U. Armbruster, W. Grünert, A. Brückner, Efficient $VO_x/Ce_{1-x}Ti_xO_2$ Catalysts for Low-Temperature NH_3-SCR: Reaction Mechanism and Active Sites Assessed by in Situ/Operando Spectroscopy, ACS Catal. 7 (2017) 1693–1705.
[78] R. Jin, Y. Liu, Y. Wang, W. Cen, Z. Wu, H. Wang, X. Weng, The role of cerium in the improved SO_2 tolerance for NO reduction with NH_3 over $Mn-Ce/TiO_2$ catalyst at low temperature, Appl. Catal. B Environ. 148–149 (2014) 582–588.
[79] L. Zhang, L. Li, Y. Cao, X. Yao, C. Ge, F. Gao, Y. Deng, C. Tang, L. Dong, Getting insight into the influence of SO_2 on TiO_2/CeO_2 for the selective catalytic reduction of NO by NH_3, Appl. Catal. B Environ. 165 (2015) 589–598.
[80] G. Marban, Mechanism of low-temperature selective catalytic reduction of NO with NH_3 over carbon-supported Mn_3O_4 Role of surface NH_3 species: SCR mechanism, J. Catal. 226 (2004) 138–155.